Computers in Biology and Medicine 139 (2021) 104984

Contents lists available at ScienceDirect

Computers in Biology and Medicine

journal homepage: www.elsevier.com/locate/compbiomed

COVID-19 X-ray image segmentation by modified whale optimization algorithm with population reduction

Sanjoy Chakraborty [a,b], Apu Kumar Saha [c,*], Sukanta Nama [d], Sudhan Debnath [e]

[a] *Department of Computer Science and Engineering, National Institute of Technology, Agartala, Tripura, India*
[b] *Department of Computer Science and Engineering, Iswar Chandra Vidyasagar College, Belonia, Tripura, India*
[c] *Department of Mathematics, National Institute of Technology, Agartala, Tripura, India*
[d] *Department of Applied Mathematics, Maharaja Bir Bikram University, Agartala, Tripura, India*
[e] *Department of Chemistry, Maharaja Bir Bikram College, Agartala, Tripura, India*

ARTICLE INFO

Keywords:
Whale optimization algorithm
Image segmentation
Multilevel thresholding
Kapur's entropy
COVID-19 chest X-ray image

ABSTRACT

Coronavirus disease 2019 (COVID-19) has caused a massive disaster in every human life field, including health, education, economics, and tourism, over the last year and a half. Rapid interpretation of COVID-19 patients' X-ray images is critical for diagnosis and, consequently, treatment of the disease. The major goal of this research is to develop a computational tool that can quickly and accurately determine the severity of an illness using COVID-19 chest X-ray pictures and improve the degree of diagnosis using a modified whale optimization method (WOA). To improve the WOA, a random initialization of the population is integrated during the global search phase. The parameters, coefficient vector (A) and constant value (b), are changed so that the algorithm can explore in the early stages while also exploiting the search space extensively in the latter stages. The efficiency of the proposed modified whale optimization algorithm with population reduction (mWOAPR) method is assessed by using it to segment six benchmark images using multilevel thresholding approach and Kapur's entropy-based fitness function calculated from the 2D histogram of greyscale images. By gathering three distinct COVID-19 chest X-ray images, the projected algorithm (mWOAPR) is utilized to segment the COVID-19 chest X-ray images. In both benchmark pictures and COVID-19 chest X-ray images, comparisons of the evaluated findings with basic and modified forms of metaheuristic algorithms supported the suggested mWOAPR's improved performance.

1. Introduction

A new virus, severe acute respiratory syndrome coronavirus 2 (SARS-CoV-2), was discovered in late December 2019 as the cause of a severe pneumonia infection outbreak identified as coronavirus disease 2019 (COVID-19). The disease reportedly arose in Wuhan City, Hubei Province, China, and was later labeled a pandemic by the World Health Organization on March 11, 2020. (WHO) [1,2]. Due to SARS-highly CoV-2's human-to-human contagious nature, the disease has affected 186.0849 million people across the world, with 4.0213 million deaths in 222 nations and territories, as well as international transportation, in the last year and a half (https://www.worldometers.info/coronavirus/). To regulate or prevent COVID-19, Li et al. [3] suggested vaccinations, monoclonal antibodies, oligonucleotide-based therapeutics, peptides, interferon therapy, and small-molecule medicines. Early identification of the disease and degree of infection, i.e., the severity of the patients, is another significant factor in combating COVID-19. The diagnosis options on the market are based on the detection of viral genes, human antibodies, and viral antigens [4]. Currently, the detection techniques of COVID-19 are real-time reverse transcription-polymerase chain reaction (RT-PCR), reverse-transcription loop-mediated isothermal amplification (RT-LAMP), specific high-sensitivity enzymatic reporter unlocking (SHERLOCK) assay, CT scan, antigen test, and serology tests [5]. The concentration of numerous biomarkers, including C-reactive protein, D-dimer, lymphocytes, leukocytes, and blood platelets, may also be useful in detecting infection and measuring illness severity [6]. In radiology, most of the literature concentrated on CT manifestations of COVID-19 [7,8]. However, because CT is not widely available, has problems with sterilization thereafter, reduces infection, and is more expensive than X-ray, portable chest X-ray is more appropriate, despite

* Corresponding author.
E-mail addresses: sanjoymtch@gmail.com (S. Chakraborty), apusaha_nita@yahoo.co.in (A.K. Saha), sukanta1122@gmail.com (S. Nama), bcsdebnath@gmail.com (S. Debnath).

https://doi.org/10.1016/j.compbiomed.2021.104984
Received 9 August 2021; Received in revised form 9 October 2021; Accepted 23 October 2021
Available online 30 October 2021

```
Initialize the population and necessary parameters
Find fitness of every solution in the population
Find the best fitness and corresponding position vector
While it < maxit do the following
    Calculate β
    For each solution in the population do the following
        Update A, C, b, l and p
            If rand < A
                If p < 0.5
                    S^{t+1} = lb + (ub − lb) * rand
                Else
                    Calculate S^{t+1} using Eqn. 6
                End if
            Else
                Calculate S^{t+1} using Eqn. 8
            End if
    End for
    Calculate population for next iteration using Eqn. 12
    Find fitness of every solution in the population
    Find best fitness and corresponding solution
    it = it + 1
End while
Return best fitness and corresponding solution
```

Fig. 1. Pseudo code of the proposed mWOAPR.

being less sensitive.

COVID-19 might be difficult to identify in some individuals due to hazy pulmonary opacities on portable chest radiography (CXR). Irregular, patchy, hazy, reticular, and extensive ground-glass opacities have been seen on the CXR of probable COVID-19 sufferers [9]. To reduce the death rate of COVID-19 patients, a faster quantitative evaluation of disease severity is essential. The interpretation of X-ray scans is one of the most challenging aspects of COVID-19 diagnosis. Several studies used artificial intelligence on X-ray images to detect COVID-19 early and accurately to tackle these challenges. Artificial intelligence has made significant progress in COVID-19 diagnostic imaging in the latest days [10,11]. Several researches have investigated to increase the diagnostic quality of COVID-19 based on X-ray picture segmentation using swarm intelligence, deep learning, deep neural networks, and neural network optimization methods [12–19]. When a patient's RT-PCR test for COVID-19 is negative early on, the other diagnosis tool, chest imaging, will play a critical role. Early detection with COVID-19 requires a high-resolution CT scan of the patient's chest. The chest CT has better sensitivity for COVID-19 diagnosis than the RT-PCR [20,21]. As a result, diagnosing COVID-19 patients from CT or X-ray pictures is critical, and tremendous advances in imaging utilizing Artificial Intelligence (AI) have been accomplished in recent years [22,23].

Swarm-based methods have shown significant performance in solving numerous practical issues [24]. Segmentation of medical images using swarm-based optimization methods is a popular application. Complex feature spaces, especially in the medical image, are often highly challenging to handle [25]. Clinical analysis is regularly inspired by just a particular segment of a medical image, while different parts are of optional significance [26]. Hence more emphasis is required on the accuracy and efficiency of the method used to handle the issue [27]. A swarm-based optimization method with efficacy can be highly effective in segmentation medical images [24]. Li et al. [28] proposed a dynamic-context cooperative quantum-behaved particle swarm optimization algorithm to segment medical images with enhanced searchability. Turajlić [29] applied firefly and bat algorithms to segment X-ray images with multilevel thresholding strategy. Abdel-Basset et al. [30] developed a new algorithm named HSMA_WOA integrating slime mould algorithm and WOA, also segmented COVID-19 chest X-ray images applying multilevel thresholding strategy. Zhao et al. [26] proposed an improved slime mould algorithm (DASMA) with a diffusion mechanism and an association strategy to increase solution diversity and faster convergence speed, respectively. They applied the method to segment the CT image of chronic obstructive pulmonary disease (COPD) using multilevel thresholding approach. Liu et al. [12] modified the ant colony optimization (ACO) algorithm using Cauchy mutation to enhance the searching ability and convergence speed of ACO. Greedy Levy mutation was used to avoid the local solution. The authors segmented the COVID-19 X-ray images applying the method with Kapur's entropy-based multilevel thresholding approach. Murillo-Olmos et al. [31] segmented X-ray images of pneumonia with whale optimization algorithm. Abualigah et al. [32] proposed differential evolution-based arithmetic optimization algorithm (DAOA). Differential evolution was used to enhance the local search, COVID-19 CT images segmented using multilevel thresholding strategy. Thus, segmentation of the COVID-19 chest X-ray images to separate the background and target by classifying image pixels can be very important to diagnose and examine the severity of a patient infected with COVID-19. This can help specialists to make a suitable conclusion and give a treatment plan. Moreover, the segmented image can be used to train the machine learning algorithms and generate decisions effectively.

Mirjalili and Lewis devised the whale optimization algorithm in 2016 while researching humpback whale feeding behavior. With only a few algorithm-specific parameters, WOA is a simple yet powerful system. Despite a few limitations, the effectiveness of WOA outperforms a few other well-known algorithms in terms of exploitation and avoiding the local optimal solution [33]. However, the conventional WOA may be trapped into a local solution due to low exploration capacity, and the best optimal solution may not be attained while solving complex problems [34]. Moreover, in WOA, global and local search phases are not well-balanced because exploitation gets higher preference in the second half of the search process [28]. As a result, this study offers mWOAPR, a novel variant of WOA that increases the algorithm's exploration capability while balancing global and local search features. In furthermore, the proposed technique has been successfully used to tackle the image segmentation problem. 2D histograms made of greyscale images are used as the fitness function to achieve an ideal threshold set, and 2D Kapur's entropy is being used as a fitness function. Hereunder are the study's main contributions:

(i) A new traversing parameter β is introduced to balance between exploration and exploitation.
(ii) Instead of the search prey phase of WOA, random initialization of solution is performed to increase exploration.
(iii) In the encircling prey and bubble-net attack phases, the value of co-efficient vector A and constant b is altered. It facilitates the exploration of the search space at the start of the process, and as iteration advances, a thorough local search is executed.

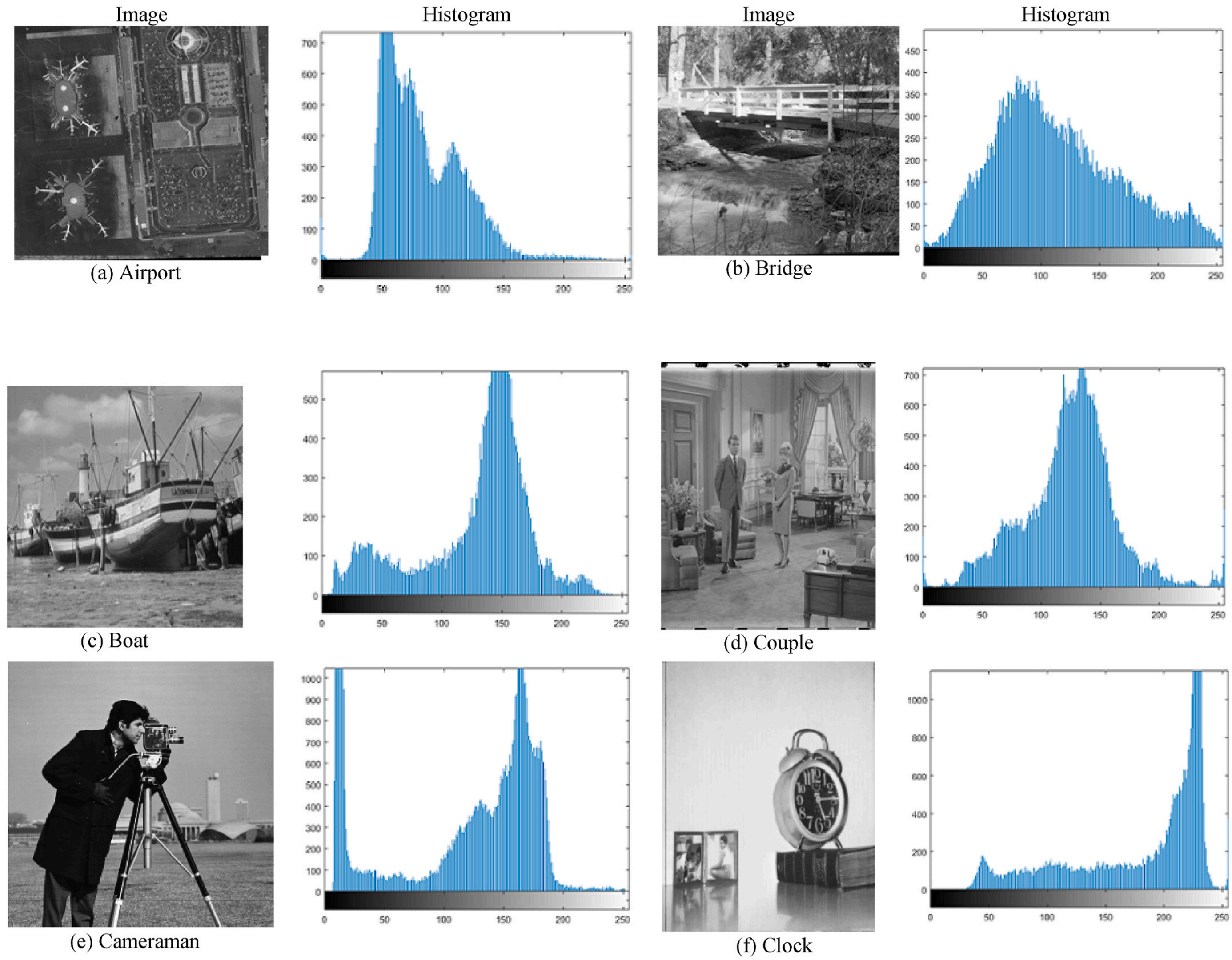

Fig. 2. Images used in the experiment of image segmentation.

(iv) A population reduction mechanism minimizes the algorithm's computational complexity and enhances the exploitation ability.
(v) Six benchmark images and three COVID-19 X-ray images are segmented using different thresholds, and evaluated results are compared with several metaheuristic algorithms.
(vi) Friedman's test, a nonparametric statistical test, has been used to validate the suggested algorithm's statistical performance. Convergence graphs are also used to assess the algorithm's solution searching capability.

The remainder of the paper is structured as follows: The description of the classic WOA is presented in Section 2. In Section 3, the proposed algorithm mWOAPR is described. In Section 4, the image segmentation problem is defined. Section 5 compares and analyses the evaluated outcomes. The algorithm's computing complexity, statistical analysis of the findings, and convergence analysis are all shown in Section 6. The research comes to a close with Section 7.

2. Whale optimization algorithm

For constructing the algorithm, the whale optimization algorithm (WOA) mimics the foraging behavior of humpback whales. WOA's execution procedure, like that of other population-based algorithms, begins with the generation of a set of random solutions. WOA's search technique is primarily divided into three stages: searching the prey, encircling the prey, and spiral bubble-net attack. WOA employs these three approaches to achieve an appropriate equilibrium between both the exploratory and exploitative processes. Finally, the search procedure ends when a pre-defined condition is met and the optimization results are produced.

2.1. Searching the prey phase

Whales randomly search the target in the search space based on their current location. The program uses the food-finding mechanism of whales to explore the search region. The mathematical formulation of this behavior is given by:

$$\overline{Dis} = \left| C.\, S_{rnd}^{(t)} - S^{(t)} \right| \tag{1}$$

$$S^{(t+1)} = S_{rnd}^{(t)} - A.\overline{Dis} \tag{2}$$

where, S represents the solution vector, S_{rnd} is a randomly chosen solution from the current solutions, and t represents the present iteration number. $\overline{Dis}$ represents the distance of random and the current solution. (.) characterizes the element-by-element multiplication, and | | signifies absolute value.

Parameters A, and C in Eqns. (1) and (2) are said to be co-efficient

Table 1
Comparison of results using image airport.

Algorithm	Image	Level	Intensity						Mean	Std	PSNR	SSIM	Best
mWOAPR	a	3	93	165	256				17.7462	1.39E-05	13.1548	0.3229	17.7462
WOA			93	165	256				17.746	6.15E-04	13.1548	0.3229	17.7462
ACWOA			93	165	256				17.7407	0.0122	13.1548	0.3229	17.7462
AWOA			93	165	256				17.7446	0.0034	13.1548	0.3229	17.7462
HIWOA			93	165	256				17.7318	0.0173	13.1548	0.3229	17.7462
ESSAWOA			95	165	256				17.6291	0.1021	13.0568	0.314	17.7417
WOAmM			93	165	256				17.7462	1.08E-14	13.1548	0.3229	17.7462
m-SDWOA			93	165	256				17.7462	1.08E-14	13.1548	0.3229	17.7462
MPBOA			91	165	256				17.7253	0.0125	15.2759	0.073	17.7461
HBO			91	163	242				17.366	0.2128	15.2809	0.0733	17.6363
HGS			93	165	256				17.7443	0.0046	15.2426	0.0713	17.7462
SMA			93	165	256				17.7462	0	15.2426	0.0713	17.7462
mWOAPR	a	4	90	153	199	256			22.1706	0.0033	13.384	0.3442	22.1729
WOA			90	153	199	256			22.1704	0.003	13.384	0.3442	22.1729
ACWOA			89	153	199	256			22.1375	0.0283	13.4404	0.3479	22.1717
AWOA			90	153	199	256			22.1683	0.0066	13.384	0.3442	22.1729
HIWOA			91	153	199	256			22.123	0.0356	13.3329	0.3438	22.172
ESSAWOA			95	153	203	256			21.847	0.2767	13.1235	0.3219	22.1356
WOAmM			90	153	199	256			22.1701	0.0021	13.384	0.3442	22.1729
m-SDWOA			90	153	199	256			22.1692	0.0034	13.384	0.3442	22.1729
MPBOA			90	153	199	256			22.1702	0.0091	15.319	0.0762	22.1729
HBO			84	157	199	250			21.383	0.3399	15.4471	0.0801	22.0295
HGS			90	153	199	256			22.1614	0.0203	15.319	0.0762	22.1729
SMA			90	153	199	256			22.1701	0.002	15.319	0.0762	22.1729
mWOAPR	a	5	82	121	160	204	256		26.2943	0.0031	14.4122	0.4181	26.2972
WOA			82	121	160	204	256		26.293	0.006	14.4122	0.4181	26.2972
ACWOA			82	126	165	207	256		26.2417	0.0545	14.3483	0.4133	26.2917
AWOA			82	121	160	204	256		26.2914	0.0048	14.4122	0.4181	26.2972
HIWOA			82	126	165	207	256		26.2391	0.0468	14.3483	0.4173	26.2917
ESSAWOA			82	129	166	204	256		25.6354	0.47	14.3081	0.4098	26.2443
WOAmM			82	121	160	204	256		26.2937	0.002	14.4122	0.4181	26.2972
m-SDWOA			82	121	160	204	256		26.2922	0.0032	14.4122	0.4181	26.2972
MPBOA			82	121	160	204	256		26.2939	0.001	15.6618	0.0908	26.2972
HBO			81	135	161	199	255		25.3102	0.4337	15.6276	0.089	26.1144
HGS			82	121	160	204	256		26.2644	0.0375	15.6618	0.0908	26.2972
SMA			82	121	160	204	256		26.2944	0.002	15.6618	0.0908	26.2972
mWOAPR	a	6	41	85	127	165	207	256	30.0772	0.0788	20.8625	0.7944	30.1577
WOA			41	85	127	165	207	256	30.068	0.0673	20.8625	0.7944	30.1577
ACWOA			41	80	121	167	206	256	29.8909	0.0908	21.4447	0.8057	30.0789
AWOA			41	85	126	165	208	256	30.0166	0.0379	20.9127	0.7944	30.1547
HIWOA			41	80	122	160	204	256	29.8993	0.0878	21.4234	0.7526	30.1442
ESSAWOA			75	122	153	183	211	256	29.3352	0.4269	15.2383	0.459	29.8886
WOAmM			41	82	121	160	204	256	30.0764	0.0713	21.374	0.8056	30.1552
m-SDWOA			41	85	127	165	207	256	30.0677	0.0825	20.8625	0.7944	30.1577
MPBOA			41	85	127	165	207	256	30.01	0.0683	17.8119	0.1141	30.1577
HBO			40	82	145	162	203	247	28.8162	0.4284	17.4326	0.1067	29.4463
HGS			41	85	122	165	208	256	29.9346	0.1072	17.8884	0.1149	30.14
SMA			41	84	124	165	207	256	30.0555	0.0756	17.8822	0.1144	30.1566

vectors and are obtained by the following equations:

$$A = 2a_1 \times rnd - a_1 \tag{3}$$

$$C = 2 \times rnd \tag{4}$$

where, a_1 declines linearly from 2 to 0 with each iteration, and *rnd* is a random number between 0 and 1.

2.2. Encircling the prey

The algorithm employs this whale hunting method for the aim of exploitation. The current best solution is anticipated to be the solution closest to the ideal value during this phase. The population's other solutions change their places concerning the current best option. The mathematical expressions to formulate this behavior are given below:

$$\overline{Dis} = \left|C.\, S_{best}^{(t)} - S^{(t)}\right| \tag{5}$$

$$S^{(t+1)} = S_{best}^{(t)} - A.\overline{Dis} \tag{6}$$

where S_{best} characterizes the best solution based on the fitness value among the whales till the present iteration.

2.3. Bubble-net attack

To approach their target, humpback whales employ a spiral-shaped route of bubbles. For local search, the bubble-net attacking technique is used. The bubble-net procedure is carried out as follows:

$$D^* = |S_{best}^{(t)} - S^{(t)}| \tag{7}$$

$$S^{(t+1)} = D^* \cdot e^{bl} \cdot cos(2\pi l) + S_{best}^{(t)} \tag{8}$$

where b denotes the shape of the logarithmic spiral path and is kept constant; l is a random number calculated using the following equation:

$$l = (a_2 - 1)\ rnd + 1 \tag{9}$$

In Eqn. (9), a_2 decreases linearly from (−1) to (−2) with each iteration and $rnd \in [0,\ 1]$.

The coefficient parameter A is used to make the transition between the algorithm's explorative and exploitative phases. When $|A| \geq 1$, the exploratory process is chosen, and the global search is started through

Table 2
Comparison of results using image bridge.

Algorithm	Image	Level	Intensity						Mean	Std	PSNR	SSIM	Best
mWOAPR	b	3	102	179	256				18.6516	0	12.9608	0.4051	18.6516
WOA			102	179	256				18.6515	3.8572e-04	12.9608	0.4051	18.6516
ACWOA			102	179	256				18.6498	0.0022	12.9608	0.4051	18.6516
AWOA			102	179	256				18.6516	4.1353e-05	12.9608	0.4050	18.6516
HIWOA			102	179	256				18.6494	0.0021	12.9608	0.4039	18.6516
ESSAWOA			106	180	256				18.5940	0.0980	12.6903	0.3900	18.6469
WOAmM			102	179	256				18.6516	2.4744e-05	12.9608	0.4051	18.6516
m-SDWOA			102	179	256				18.6516	0	12.9608	0.4051	18.6516
MPBOA			103	179	256				18.6361	0.0108	13.1722	0.0699	18.6514
HBO			94	172	255				18.3728	0.1687	13.4228	0.0767	18.6140
HGS			102	179	256				18.6515	0.0003	13.1944	0.0706	18.6516
SMA			102	179	256				18.6516	0	13.1944	0.0706	18.6516
mWOAPR	b	4	63	130	195	256			23.4015	3.3610e-04	16.7992	0.6241	23.4017
WOA			63	130	195	256			23.4014	0.0013	16.7992	0.6241	23.4017
ACWOA			63	131	195	256			23.3845	0.0174	16.7661	0.6218	23.4006
AWOA			63	130	195	256			23.4006	0.0020	16.7992	0.6241	23.4017
HIWOA			63	130	195	256			23.3835	0.0164	16.7992	0.6194	23.4017
ESSAWOA			64	127	194	256			23.1809	0.1933	16.9415	0.6317	23.3916
WOAmM			63	130	195	256			23.4013	7.1123e-04	16.7992	0.6241	23.4017
m-SDWOA			63	130	195	256			23.4014	5.4523e-04	16.7992	0.6241	23.4017
MPBOA			64	130	193	256			23.3571	0.0376	14.4922	0.0955	23.3954
HBO			6	129	195	254			22.8525	0.2589	14.3361	0.0934	23.2965
HGS			63	130	195	256			23.3946	0.0094	14.4739	0.0954	23.4017
SMA			63	130	195	256			23.4015	0.0005	14.4739	0.0954	23.4017
mWOAPR	b	5	55	103	150	199	256		27.7540	0.0011	19.0347	0.7366	27.7545
WOA			55	103	150	199	256		27.7537	0.0012	19.0347	0.7366	27.7545
ACWOA			55	103	151	199	256		27.7059	0.0659	19.0226	0.7356	27.7540
AWOA			55	103	150	199	256		27.7534	0.0011	19.0347	0.7356	27.7545
HIWOA			57	106	153	201	256		27.6765	0.0590	18.9485	0.7349	27.7492
ESSAWOA			54	116	165	207	256		27.2720	0.3224	18.1740	0.6958	27.6681
WOAmM			55	103	150	199	256		27.7533	0.0011	19.0347	0.7366	27.7545
m-SDWOA			55	103	150	199	256		27.7529	0.0017	19.0347	0.7366	27.7545
MPBOA			55	107	154	204	256		27.6921	0.0418	15.1572	0.1030	27.7404
HBO			48	100	169	211	253		26.8619	0.3619	14.8889	0.1023	27.4814
HGS			54	101	149	199	256		27.7259	0.0236	15.2325	0.1033	27.7522
SMA			55	103	150	199	256		27.7531	0.0024	15.2190	0.1031	27.7545
mWOAPR	b	6	52	92	132	172	211	256	31.7673	7.3212e-04	20.4208	0.7857	31.7680
WOA			52	92	132	172	211	256	31.7670	8.2313e-04	20.4208	0.7857	31.7680
ACWOA			53	94	135	179	217	256	31.6674	0.0907	20.1722	0.7754	31.7559
AWOA			52	92	132	172	211	256	31.7668	0.0013	20.4208	0.7857	31.7680
HIWOA			49	92	135	173	211	256	31.6397	0.1091	20.2724	0.7813	31.7617
ESSAWOA			50	85	141	187	217	256	31.0189	0.3644	19.6431	0.7545	31.5843
WOAmM			52	92	132	172	211	256	31.7667	0.0013	20.4208	0.7857	31.7680
m-SDWOA			52	92	132	172	211	256	31.7657	0.0026	20.4208	0.7857	31.7680
MPBOA			52	92	134	174	209	256	31.6845	0.0472	15.6622	0.1060	31.7455
HBO			20	52	65	121	161	237	30.6683	0.4360	15.2443	0.1011	31.4979
HGS			49	93	135	175	212	256	31.6841	0.0628	15.6150	0.1067	31.7589
SMA			52	92	132	172	211	256	31.7600	0.0159	15.6811	0.1062	31.7680

Eqn. (1) and Eqn. (2). If $|A| < 1$, the candidate whales upgrade positions by Eqn. (6) or Eqn. (8) depending on a probability value α, which is constant ($\alpha = 0.5$), and based on the value of α, the search process transits between encircling prey or bubble-net attacking strategy. The mathematical representation of the same is given below:

$$\begin{cases} S^{(t+1)} = S^{t}_{best} - A.\,\overline{Dis} & if\ \alpha\ <\ 0.5 \\ S^{(t+1)} = D^{*}\cdot e^{bl}\cos(2\pi l) + S^{t}_{best} & if\ \alpha \geq 0.5 \end{cases} \tag{10}$$

3. Proposed modified WOA with population reduction (mWOAPR)

The humpback whale's hunting behavior inspired the development of whale optimization algorithm. The whales migrate while hunting for food, selecting a random solution from the population; this phase has been termed the search for prey phase. The algorithm's global search phase led this phase. Local searches were conducted by encircling the target and using the whale's bubble-net attack strategy. The solutions in both of these phases were updated using the current best value. To search away from the current solution, two co-efficient vectors A and C, are employed. In basic WOA, selection between exploration and exploitation were performed using the value of co-efficient vector A, and an arbitrary number p. The arrangement steered the search process only to the exploitation phase during the second part of the search [35], decreasing diversity in the solution.

In the proposed mWOAPR, a new selection parameter β is introduced, which varies between 1 and 0. Selection between the exploration and exploitation phase is achieved using the value of β. The parameters $A$and b used in classical WOA are also modified here. An arbitrary number is subtracted from β to get the value of A. While exploiting the search space using the bubble-net method, the value of β is used instead of 1 in WOA. β is calculated using the equation below:

$$\beta = 1 - iter/maxiter \tag{11}$$

In the above equation, *iter* and *maxiter* represent the present iteration value and the maximum number of iterations, respectively.

Like other metaheuristic algorithms, mWOAPR starts with initializing a random population. If the value of β is greater than a random number and another random number is less than 0.5, the exploration phase is selected. Unlike the WOA search for prey phase in the exploration phase, the present solution is regenerated to increase the exploration. Otherwise, the encircling prey phase in Eqn. (6) is used. The

Table 3
Comparison of results using image boat.

Algorithm	Image	Level	Intensity						Mean	Std	PSNR	SSIM	Best
mWOAPR	c	3	109	180	256				18.1487	5.81E-04	14.7695	0.5468	18.1488
WOA			109	180	256				18.1482	0.0018	14.7695	0.5468	18.1488
ACWOA			109	180	256				18.1449	0.0067	14.7695	0.5468	18.1488
AWOA			109	180	256				18.1476	0.0026	14.7695	0.5468	18.1488
HIWOA			109	180	256				18.1433	0.0074	14.7695	0.5468	18.1488
ESSAWOA			105	181	256				18.0577	0.0852	14.5654	0.5459	18.1435
WOAmM			109	180	256				18.1483	3.51E-05	14.7695	0.5468	18.1488
m-SDWOA			109	180	256				18.1487	2.64E-14	14.7695	0.5468	18.1488
MPBOA			107	180	254				18.1396	0.0083	13.242	0.0548	18.1486
HBO			102	179	247				17.8082	0.2466	13.155	0.0549	18.1208
HGS			109	180	256				18.1483	0.0023	13.2674	0.0549	18.1488
SMA			109	180	256				18.1487	0	13.2674	0.0549	18.1488
mWOAPR	c	4	65	122	181	256			22.8344	9.47E-04	17.8699	0.6682	22.8346
WOA			65	122	181	256			22.8341	0.0011	17.8699	0.6682	22.8346
ACWOA			64	122	181	256			22.8201	0.0111	17.8736	0.6681	22.8344
AWOA			65	122	181	256			22.8342	0.0014	17.8699	0.6682	22.8346
HIWOA			65	122	181	256			22.8209	0.0143	17.8699	0.6682	22.8346
ESSAWOA			61	122	182	256			22.6667	0.1195	17.8266	0.6668	22.8156
WOAmM			65	122	181	256			22.8342	1.19E-04	17.8699	0.6682	22.8346
m-SDWOA			65	122	181	256			22.8341	1.36E-04	17.8699	0.6682	22.8346
MPBOA			64	122	181	256			22.8177	0.0159	14.3021	0.0619	22.8344
HBO			66	114	179	250			22.2441	0.3373	14.0333	0.0599	22.777
HGS			65	122	181	256			22.8304	0.0067	14.3009	0.0618	22.8346
SMA			65	122	181	256			22.834	0.0002	14.3009	0.0618	22.8346
mWOAPR	c	5	51	92	130	181	256		26.9507	0.025	20.0294	0.7344	26.9576
WOA			51	92	130	181	256		26.9477	0.0262	20.0294	0.7344	26.9576
ACWOA			52	91	130	181	254		26.8855	0.0629	19.9857	0.7321	26.9559
AWOA			51	92	130	181	256		26.927	0.0511	20.0294	0.7344	26.9576
HIWOA			52	91	130	181	256		26.8948	0.0582	19.9857	0.731	26.9559
ESSAWOA			51	97	131	180	248		26.5258	0.2742	20.2102	0.7388	26.921
WOAmM			51	92	130	181	256		26.9507	0.0044	20.0294	0.7344	26.9576
m-SDWOA			51	92	130	181	256		26.9502	0.0018	20.0294	0.7344	26.9576
MPBOA			53	92	130	181	256		26.9247	0.0215	15.0047	0.0646	26.9554
HBO			61	99	132	190	240		26.0944	0.3704	14.9467	0.0626	26.7732
HGS			53	92	130	181	256		26.8567	0.0704	15.0047	0.0646	26.9554
SMA			51	92	130	181	256		26.9501	0.0015	15.0207	0.0651	26.9576
mWOAPR	c	6	50	90	128	166	195	256	30.8696	0.0058	21.0599	0.7595	30.8762
WOA			50	90	128	166	195	256	30.8683	0.0093	21.0599	0.7595	30.8762
ACWOA			50	89	128	166	195	256	30.827	0.0474	21.0384	0.7587	30.8752
AWOA			50	91	128	166	195	256	30.8663	0.0085	21.0782	0.7595	30.8757
HIWOA			49	88	125	166	195	256	30.7777	0.1017	20.7002	0.764	30.8658
ESSAWOA			50	92	129	172	205	256	30.1745	0.3845	20.6883	0.7457	30.8456
WOAmM			50	90	128	166	195	256	30.869	0.0115	21.0599	0.7595	30.8762
m-SDWOA			50	90	128	166	195	256	30.8676	0.0116	21.0599	0.7595	30.8762
MPBOA			52	91	128	166	196	256	30.8417	0.0161	15.3534	0.0671	30.8696
HBO			58	85	128	165	190	254	29.8476	0.4058	15.2249	0.0657	30.6438
HGS			50	90	125	166	195	256	30.8126	0.0448	15.2461	0.0671	30.8652
SMA			50	90	128	166	195	256	30.867	0.0063	15.3643	0.0676	30.8762

value of A is restricted within the range $[-1, 1]$ only to exploit the positions around the best value. While β is less than an arbitrary value, then the bubble-net attack phase is selected. The radius of the spiral path decreases gradually, and the variable $b$defines the shape of the spiral path, considering that value of b is taken within $[-1, 1]$ instead of 1 in WOA. After updating solutions in an iteration, the population for the next iteration is calculated using the formula given in Eqn. (12).

$$New_{pop} = round\left\{\left(\frac{minpop - pop}{maxnfes}\right) * nfes + pop\right)\right\} \tag{12}$$

In Eqn. (12), *pop* signifies the population value, *minpop* is the minimum number of solutions the population may decrease. *nfes* is the current value of function evaluation, and *maxnfes* is the maximum number of function evaluations. While experimenting, we have fixed *minpop* value to 15. Reduction of the population reduces complexity and increases convergence speed and local search ability of the algorithm. The best fitness value is returned as output. The pseudo-code of the proposed algorithm is given in Fig. 1.

3.1. Steps involved in mWOAPR

The stepwise execution process of mWOAPR is given below:

1. Initialize the random population and other related parameters.
2. Evaluate each solution's fitness and find the present best fitness and the best solution.
3. Calculate the traversing parameter β.
4. Evaluate update value of A, C, b *and* l
5. If the value of A is greater than a random value and also a random value is greater than 0.5 then reinitialize the current solution.
6. If the value of A is greater than a random value and also a random value is less than or equal to 0.5 then update the current solution using the encircling prey strategy.
7. If the value of A is less than or equal to a random value, update the current solution using the bubble-net attack method.
8. Update each solution in the population using either step 5, step 6, or step 7.
9. Evaluate the value of the new population after reduction using equation (12).

Table 4
Comparison of results using image couple.

Algorithm	Image	Level	Intensity						Mean	Std	PSNR	SSIM	Best
mWOAPR	d	3	99	182	255				18.0654	3.61E-15	14.3523	0.5021	18.0654
WOA			99	182	255				18.065	5.90E-04	14.3523	0.5021	18.0654
ACWOA			99	182	255				18.0496	0.0156	14.3523	0.5021	18.0654
AWOA			99	182	255				18.0651	4.57E-04	14.3523	0.5021	18.0654
HIWOA			99	180	255				18.0405	0.0105	14.3402	0.5025	18.0644
ESSAWOA			97	183	255				17.936	0.1061	14.3134	0.5013	18.0572
WOAmM			99	182	255				18.065	0.0016	14.3523	0.5021	18.0654
m-SDWOA			99	182	255				18.0653	2.57E-04	14.3523	0.5021	18.0654
MPBOA			99	182	255				18.0654	0	13.4599	0.053	18.0654
HBO			106	177	250				17.6444	0.2063	13.4308	0.0552	17.9184
HGS			99	182	255				18.0374	0.0229	13.4599	0.053	18.0654
SMA			99	182	255				18.0652	0.0006	13.4599	0.053	18.0654
mWOAPR	d	4	93	159	201	254			22.6356	0.0161	15.1245	0.551	22.6542
WOA			93	159	201	254			22.6349	0.017	15.1245	0.551	22.6542
ACWOA			94	162	201	254			22.576	0.0569	14.9996	0.546	22.6369
AWOA			93	159	201	254			22.6355	0.0148	15.1245	0.551	22.6542
HIWOA			99	161	201	254			22.5618	0.0598	15.0251	0.6659	22.6379
ESSAWOA			99	161	206	254			22.4293	0.1321	15.0225	0.5445	22.5963
WOAmM			93	159	201	254			22.6348	0.015	15.1245	0.551	22.6542
m-SDWOA			93	159	201	254			22.6278	0.013	15.1245	0.551	22.6542
MPBOA			60	113	180	255			22.5493	0.0464	14.6775	0.0636	22.6122
HBO			70	100	173	253			21.8734	0.2706	14.2903	0.0573	22.2631
HGS			93	160	201	254			22.5954	0.0411	13.701	0.0581	22.6536
SMA			93	159	201	254			22.6238	0.01	13.7173	0.0584	22.6542
mWOAPR	d	5	60	107	160	201	254		27.1485	0.0168	18.8267	0.7067	27.1603
WOA			60	107	160	201	254		27.1369	0.0402	18.8267	0.7067	27.1603
ACWOA			60	107	160	201	254		27.1467	0.0183	18.8267	0.7067	27.1603
AWOA			60	108	160	201	254		27.1392	0.0184	18.8917	0.7076	27.1587
HIWOA			63	107	162	204	254		26.9531	0.1156	18.6986	0.7021	27.129
ESSAWOA			60	109	156	201	253		26.5557	0.3309	19.242	0.7129	27.0798
WOAmM			60	107	160	201	254		27.1442	0.0193	18.8267	0.7067	27.1603
m-SDWOA			60	107	160	201	254		27.1467	0.0109	18.8267	0.7067	27.1603
MPBOA			58	108	160	202	254		27.0105	0.0681	14.9586	0.0658	27.1348
HBO			57	112	155	194	254		25.9079	0.4622	15.0946	0.0682	26.8265
HGS			62	111	162	201	254		26.9607	0.1686	14.9925	0.066	27.1412
SMA			60	107	160	201	254		27.1477	0.0064	14.9513	0.0651	27.1603
mWOAPR	d	6	59	96	130	166	203	254	31.0215	0.0079	21.5266	0.7782	31.0285
WOA			59	97	131	166	203	254	31.0203	0.0086	21.387	0.7781	31.0283
ACWOA			58	101	131	165	202	254	30.8016	0.1378	21.5236	0.783	30.9914
AWOA			59	97	131	166	203	254	31.0142	0.0177	21.387	0.78	31.0283
HIWOA			58	102	137	166	203	254	30.7805	0.1087	21.107	0.778	30.9881
ESSAWOA			59	97	136	168	200	254	30.2168	0.5064	20.8817	0.7605	30.9676
WOAmM			58	97	131	166	203	254	31.0103	0.0169	21.3918	0.7783	31.0242
m-SDWOA			59	98	131	166	203	254	31.0125	0.0118	21.4316	0.78	31.0264
MPBOA			57	95	129	167	201	254	30.8519	0.092	15.7885	0.066	31.0099
HBO			58	100	134	163	198	239	29.593	0.3732	15.8458	0.0672	30.4203
HGS			59	103	137	170	204	254	30.7546	0.179	15.7111	0.0671	31.0086
SMA			59	96	129	166	203	254	31.0093	0.0184	15.8104	0.0658	31.0264

10. Move in between step 2 to step 9 as long as the termination condition is not true.
11. Return the final best fitness and the corresponding solution as output.

4. Image segmentation

Segmentation of images has been motivating researchers from various areas for years, owing to the advent of computer vision applications. In today's world, digital cameras are ubiquitous and linked to multiple devices for a variety of applications that require specific treatment for reasons such as medical diagnostics, monitoring, commercial deployments, and so on. The process of dividing a digital image into non-overlapping areas or segments and finding objects and boundaries in images is known as segmentation. The intensities of pixels within a region are homogenous or comparable in terms of properties such as grey level, texture, color, and brightness [36]. Image segmentation is regarded as a vital component in the study of computer vision and image processing systems; it impacts the entire image or a collection of object outlines in a succession of pieces and isolates the image into groups of pixels, and divides the parts along these lines in such a way that it is extremely precise [37]. Each pixel in a region is comparable in specific unique or calculated properties, such as color, texture, or intensity. Image segmentation produces many divisions that distribute the main image or collection of forms ejected from the image. The goal of segmentation is to pre-process an image to expedite future processing chores by improving the look of the original image [38]. It is critical to note that each segmentation procedure has two primary goals: decomposing the target picture into sub-images to aid in a more comprehensive analysis and modify the representation. The segmented section of a picture should be homogenous and uniform in color, grey level, texture, and simplicity. Similarly, neighboring pixels should have considerably different values. The objective of segmentation is to simplify or transform a picture into a meaningful representation that can be analyzed further.

The most popular approach for segmenting digital pictures based on histograms is the thresholding technique for image segmentation. Thresholding-based methods classify or group features based on the intensity range of the pixels. It is one of the simplest but most effective methods for segmenting images that can differentiate between objects and other parts of an image by establishing image thresholds. The most sophisticated, relevant, and fascinating image analysis and pattern

Table 5
Comparison of results using image cameraman.

Algorithm	Image	Level	Intensity						Mean	Std	PSNR	SSIM	Best
mWOAPR	e	3	128	196	256				17.5842	3.76E-13	13.6257	0.5342	17.5842
WOA			128	196	256				17.5842	4.29E-05	13.6257	0.5342	17.5842
ACWOA			128	196	256				17.5827	0.0031	13.6257	0.5342	17.5842
AWOA			128	196	256				17.5842	4.54E-05	13.6257	0.5342	17.5842
HIWOA			128	196	256				17.5723	0.0316	13.6257	0.5342	17.5842
ESSAWOA			127	196	256				17.3457	0.2257	13.7172	0.5374	17.584
WOAmM			128	196	256				17.5842	4.19E-13	13.6257	0.5342	17.5842
m-SDWOA			128	196	256				17.5842	3.27E-05	13.6257	0.5342	17.5842
MPBOA			133	196	255				17.5314	0.039	13.1195	0.5183	17.5743
HBO			117	192	255				16.7845	0.3637	14.2737	0.562	17.5034
HGS			128	196	256				17.5841	0.0002	13.6257	0.5342	17.5842
SMA			128	196	256				17.5842	0	13.6257	0.5342	17.5842
mWOAPR	e	4	44	103	196	256			21.9771	0.0483	14.4602	0.6247	22.0073
WOA			44	103	196	256			21.9669	0.0504	14.4602	0.6247	22.0073
ACWOA			44	103	196	255			21.9163	0.1129	14.4602	0.6247	22.0073
AWOA			44	103	196	256			21.9704	0.048	14.4602	0.6247	22.0073
HIWOA			44	103	196	256			21.9414	0.0591	14.4602	0.6246	22.0073
ESSAWOA			47	102	196	256			21.6785	0.2572	14.3565	0.6206	21.9929
WOAmM			44	103	196	256			21.975	0.0325	14.4602	0.6247	22.0073
m-SDWOA			44	103	196	256			22.0027	0.0195	14.4602	0.6247	22.0073
MPBOA			43	102	196	256			21.9422	0.0588	14.3425	0.6215	22.0028
HBO			28	100	199	253			21.2211	0.3588	14.0102	0.6084	21.822
HGS			44	103	196	256			21.9623	0.0464	14.4602	0.6247	22.0073
SMA			44	103	196	256			22.007	0.001	14.4602	0.6247	22.0073
mWOAPR	e	5	44	96	146	196	256		26.5831	0.0039	20.1531	0.687	26.5863
WOA			44	96	146	196	256		26.5694	0.0243	20.1531	0.687	26.5863
ACWOA			40	96	146	196	255		26.4391	0.2042	20.1357	0.6883	26.577
AWOA			44	96	146	196	256		26.5753	0.0119	20.1531	0.687	26.5863
HIWOA			44	98	147	196	256		26.442	0.1708	20.2857	0.6886	26.5812
ESSAWOA			32	95	135	198	253		25.8792	0.3325	19.0687	0.7129	26.4087
WOAmM			44	96	146	196	256		26.5814	0.004	20.1531	0.687	26.5863
m-SDWOA			44	96	146	196	256		26.5831	0.0041	20.1531	0.687	26.5863
MPBOA			45	96	144	196	255		26.4959	0.0605	20.068	0.6973	26.5781
HBO			3	52	139	154	229		25.4632	0.4509	17.2685	0.6847	26.3201
HGS			43	96	145	196	256		26.5491	0.0235	20.1136	0.6925	26.582
SMA			44	96	146	196	256		26.5822	0.0021	20.1531	0.687	26.5863
mWOAPR	e	6	24	60	98	146	196	256	30.5274	0.0506	20.6608	0.7081	30.56
WOA			24	60	98	146	196	256	30.5262	0.0459	20.6608	0.7081	30.56
ACWOA			26	67	102	146	196	256	30.357	0.105	20.9413	0.7165	30.5272
AWOA			24	60	98	146	196	256	30.5145	0.0577	20.6608	0.713	30.56
HIWOA			22	60	98	145	196	255	30.349	0.1944	20.5972	0.7194	30.5524
ESSAWOA			22	45	98	158	199	254	29.6313	0.3481	19.6474	0.6504	30.15
WOAmM			24	61	98	146	196	256	30.5264	0.052	20.6618	0.7077	30.5599
m-SDWOA			24	60	98	146	196	256	30.5196	0.0471	20.6608	0.7081	30.56
MPBOA			23	61	100	142	197	255	30.4354	0.0548	20.4607	0.7294	30.5255
HBO			31	85	129	200	224	255	29.065	0.4983	18.1932	0.7092	29.9247
HGS			22	59	100	148	197	256	30.3791	0.0901	20.8259	0.7025	30.5345
SMA			24	61	98	146	196	256	30.5062	0.0727	20.6618	0.7077	30.5599

detection approach is automatic image separation [39]. Image segmentation methods are classified into two types based on their thresholds: parametric and nonparametric [40]. Because they involve the analysis of a probability density function, parametric methods are time-demanding. On the other hand, nonparametric methods are more precise and dependable and do not involve estimating any probability function. The techniques for nonparametric strategies are established based on statistical skills that aid in analyzing histogram data; these tools include intra-class variance, entropy, error rate, and so on. When using an optimization strategy, such statistical approaches might be employed as objective functions [41]. Threshold values can be computed when the parameter is being maximized or minimized based on its characteristics. The precision of segmentation is determined by the threshold values chosen. A histogram for the image can help with threshold selection.

Bi-level and multilevel thresholding are two different forms of thresholding [42]. In bi-level thresholding, the image pixels are categorized into two groups: (i) pixels with intensities less than the threshold and (ii) pixels greater than the threshold. On the other hand, image pixels are split into many classes in multilayer thresholding. Each class has a grey level value that is defined by several threshold values. Otsu's between class variance [43] and Kapur's entropy method [44] are two widely used techniques for image segmentation via thresholding. Otsu's between-class variance is a popular method called a global strategy due to its simplicity and efficacy. However, because it is one-dimensional and only examines information at the grey level, it does not provide a superior segmentation result [45]. On the other hand, the notion of maximizing Kapur's entropy as a metric for object segmentation is based on the premise that an image comprises a foreground and a background area with values contributing to the distribution of object intensity [45]. Both areas are computed independently to maximize their amount. The best limit value is then determined to maximize the entropy amount.

4.1. Problem formulation of multilevel thresholding

Thresholding can be bi-level or multilevel. Bi-level thresholding uses only one threshold value t_{hld} and two classes CL^0 and CL^1 are created on this threshold value. While in multilevel thresholding threshold values of n numbers are used $\{ t_{hld1}, t_{hld2} \dots \dots \dots, t_{hldn} \}$ and splits the image (I) into $(n+1)$ classes of $\{ CL^0, CL^1, CL^2, \dots \dots, CL^n \}$.

In an image I of P grey levels, bi-level thresholding can be written as:

Table 6
Comparison of results using image clock.

Algorithm	Image	Level	Intensity						Mean	Std	PSNR	SSIM	Best
mWOAPR	f	3	110	186	256				17.6289	1.45E-14	14.7191	0.7599	17.6289
WOA			110	186	256				17.6289	2.47E-14	14.7191	0.7599	17.6289
ACWOA			110	186	256				17.6264	0.004	14.7191	0.7599	17.6289
AWOA			110	186	256				17.6289	1.50E-04	14.7191	0.7599	17.6289
HIWOA			110	186	256				17.6267	0.0034	14.7191	0.7599	17.6289
ESSAWOA			110	185	256				17.5937	0.0336	14.6565	0.7606	17.6283
WOAmM			110	186	256				17.6289	1.45E-14	14.7191	0.7599	17.6289
m-SDWOA			110	186	256				17.6289	1.58E-04	14.7191	0.7599	17.6289
MPBOA			111	186	256				17.5949	0.0143	11.2156	0.0338	17.6283
HBO			9	90	174				17.4228	0.1006	11.1056	0.04	17.5943
HGS			110	186	256				17.6251	0.0104	11.2289	0.034	17.6289
SMA			110	186	256				17.6289	0	11.2289	0.034	17.6289
mWOAPR	f	4	27	110	186	256			22.3195	0.0917	15.8086	0.808	22.3838
WOA			27	110	186	256			22.31	0.0987	15.8086	0.808	22.3838
ACWOA			27	108	186	256			22.255	0.0954	15.8221	0.8089	22.3827
AWOA			27	110	186	256			22.3166	0.0114	15.8086	0.808	22.3838
HIWOA			27	112	186	256			22.2141	0.0922	15.7815	0.8076	22.3825
ESSAWOA			27	108	188	256			22.0843	0.2429	15.9541	0.8075	22.3766
WOAmM			27	110	186	256			22.3189	0.0641	15.8086	0.808	22.3838
m-SDWOA			27	110	186	256			22.3149	0.0413	15.8086	0.808	22.3838
MPBOA			26	95	162	225			22.1435	0.0884	12.0939	0.0437	22.2875
HBO			85	135	200	250			21.7855	0.214	12.2293	0.039	22.0638
HGS			27	110	186	256			22.2538	0.098	11.5921	0.0409	22.3838
SMA			27	110	186	256			22.3037	0.0004	11.5921	0.0409	22.3838
mWOAPR	f	5	27	89	142	196	256		26.9146	0.0247	18.437	0.8534	26.9269
WOA			27	89	142	196	256		26.901	0.1207	18.437	0.8534	26.9269
ACWOA			59	112	161	202	254		26.9124	0.1408	18.9517	0.7049	27.1236
AWOA			27	89	141	196	256		26.9023	0.0249	18.4264	0.8526	26.9256
HIWOA			27	89	138	196	256		26.5345	0.3021	18.3765	0.8529	26.9152
ESSAWOA			27	75	140	202	256		26.3557	0.3368	18.7322	0.8445	26.7965
WOAmM			27	89	142	196	256		26.8979	0.121	18.437	0.8534	26.9269
m-SDWOA			27	89	142	196	256		26.9083	0.0396	18.437	0.8534	26.9269
MPBOA			27	83	143	197	256		26.7304	0.1294	12.4954	0.0426	26.9017
HBO			26	79	138	179	222		25.7674	0.3446	13.2152	0.0442	26.5713
HGS			27	91	144	196	256		26.7359	0.2311	12.4643	0.0426	26.9246
SMA			27	89	142	196	256		26.9135	0.0023	12.4682	0.0426	26.9269
mWOAPR	f	6	27	77	119	160	202	256	30.9996	0.0247	20.1882	0.8725	31.018
WOA			27	77	119	160	202	256	30.9782	0.1793	20.1882	0.8725	31.018
ACWOA			27	78	115	153	201	256	30.7691	0.2263	19.9151	0.8703	30.9812
AWOA			27	79	120	158	202	256	30.9106	0.1282	20.1388	0.8714	31.0091
HIWOA			27	82	121	162	202	256	30.6499	0.3629	20.1659	0.8724	31.0045
ESSAWOA			27	80	102	152	205	256	30.1325	0.4942	19.9865	0.8559	30.682
WOAmM			27	77	119	160	202	256	30.998	0.0191	20.1882	0.8725	31.018
m-SDWOA			27	77	119	160	202	256	30.9916	0.031	20.1882	0.8725	31.018
MPBOA			27	85	125	162	206	256	30.8151	0.1093	13.1671	0.0433	30.9463
HBO			25	61	89	131	184	229	29.3527	0.5744	12.9582	0.0439	30.3689
HGS			27	78	119	163	203	256	30.7718	0.1887	13.098	0.0432	31.0039
SMA			27	77	119	160	202	256	31.0077	0.0113	13.0519	0.043	31.018

$$CL^0 = \{ f(x,y) \in I \mid 0 \le f(x,y) \le t_{hld1} - 1\}$$

$$CL^1 = \{ f(x,y) \in I \mid t_{hld} \le f(x,y) \le P - 1\}$$

where $f(x,y)$ denotes the intensity of pixels of the image I.

For multilevel image thresholding, the same equations can be stretched to

$$CL^0 = \{ f(x,y) \in I \mid 0 \le f(x,y) \le t_{hld1} - 1\}$$

$$CL^1 = \{ f(x,y) \in I \mid t_{hld1} \le f(x,y) \le t_{hld2} - 1\}$$

$$CL^3 = \{ f(x,y) \in I \mid t_{hld2} \le f(x,y) \le t_{hld3} - 1\}$$

$$CL^n = \{ f(x,y) \in I \mid t_{hldn} \le f(x,y) \le P - 1\}$$

4.2. Kapur's entropy method

Kapur's function measures the separability of the class and calculates entropy measurement using the probability distribution of the image's grey level values. The threshold's optimal values are gained whenever entropy measure in segmented classes has the highest value. The process aims to find the highest entropy value, which returns the best threshold value. Kapur's entropy was initially developed for bi-level thresholding of images. The procedure can be extended to multilevel thresholding. For bi-level thresholding, the fitness function can be written as,

$$F_1(t_{hld}) = ET_0 + ET_1 \tag{13}$$

where,

$$ET_0 = -\sum_{i=0}^{t_{hld}-1} \frac{x_i}{\omega_0} \ln\left(\frac{x_i}{\omega_0}\right), \ \omega_0 = \sum_{i=0}^{t_{hld}-1} x_i$$

$$ET_1 = -\sum_{i=t_{hld}}^{P-1} \frac{x_i}{\omega_1} \ln\left(\frac{x_i}{\omega_1}\right), \ \omega_1 = \sum_{i=t_{hld}}^{P-1} x_i$$

In the above equations ET_0 and ET_1 signify the entropies, ω_0 and ω_1 represent the class probabilities of the segmented classes CL^0 and CL^1, respectively. x_i is the probability of grey level i. x_i is calculated as follows,

$$x_i = \frac{h(\mathrm{i})}{\sum_{i=0}^{P-1} hg(i)}, \ i = 0, 1, \ldots\ldots P-1$$

Table 7
Algorithms with maximum mean fitness in different levels of benchmark images.

Image	Level	Algorithm
a	3	mWOAPR, WOAmM, m-SDWOA, SMA
	4	mWOAPR
	5	mWOAPR
	6	mWOAPR
b	3	mWOAPR, AWOA, WOAmM, m-SDWOA, SMA
	4	mWOAPR, SMA
	5	mWOAPR
	6	mWOAPR
c	3	mWOAPR, m-SDWOA, SMA
	4	mWOAPR
	5	mWOAPR, WOAmM
	6	mWOAPR
d	3	mWOAPR, MPBOA
	4	mWOAPR
	5	mWOAPR
	6	mWOAPR
e	3	mWOAPR, WOA, AWOA, WOAmM, m-SDWOA, SMA
	4	mWOAPR
	5	mWOAPR, m-SDWOA
	6	mWOAPR
f	3	mWOAPR, WOA, AWOA, WOAmM, m-SDWOA, SMA
	4	mWOAPR
	5	mWOAPR
	6	mWOAPR

where $h(\mathrm{i})$ is the histogram value of the pixel in i^{th} position.

Stretching the formula for multilevel thresholding into $(n+1)$ classes, the objective function of multilevel thresholding can be written as,

$$F_1\left(t_{hld1,}t_{hld2,\ldots\ldots\ldots\ldots,}t_{hld1,}\right) = ET_0 + ET_1 + \ldots.. + ET_n = \tag{14}$$

where,

$$ET_0 = -\sum_{i=0}^{t_{hld1}-1}\frac{x_i}{\omega_0}\ln\left(\frac{x_i}{\omega_0}\right),\ \omega_0 = \sum_{i=0}^{t_{hld1}-1}x_i$$

$$ET_1 = -\sum_{i=t_{h1}}^{t_{hld2}-1}\frac{x_i}{\omega_1}\ln\left(\frac{x_i}{\omega_1}\right),\ \omega_1 = \sum_{i=t_{h1}}^{t_{hld2}-1}x_i$$

$$ET_n = -\sum_{i=t_{hldn}}^{P-1}\frac{x_i}{\omega_n}\ln\left(\frac{x_i}{\omega_n}\right),\ \omega_n = \sum_{i=t_{hldn}}^{P-1}x_i$$

$ET_0, ET_1, \ldots. ET_n$ are the entropies, $\omega_0, \omega_{1,\ \ldots\ldots\ldots}\ \omega_n$ represents the class probabilities of the segmented classes CL^0, CL^1, …. CL^nrespectively.

4.3. Image quality measurement

Multilevel image threshold segmentation performance can be measured in several ways. This study uses peak signals to noise ratio

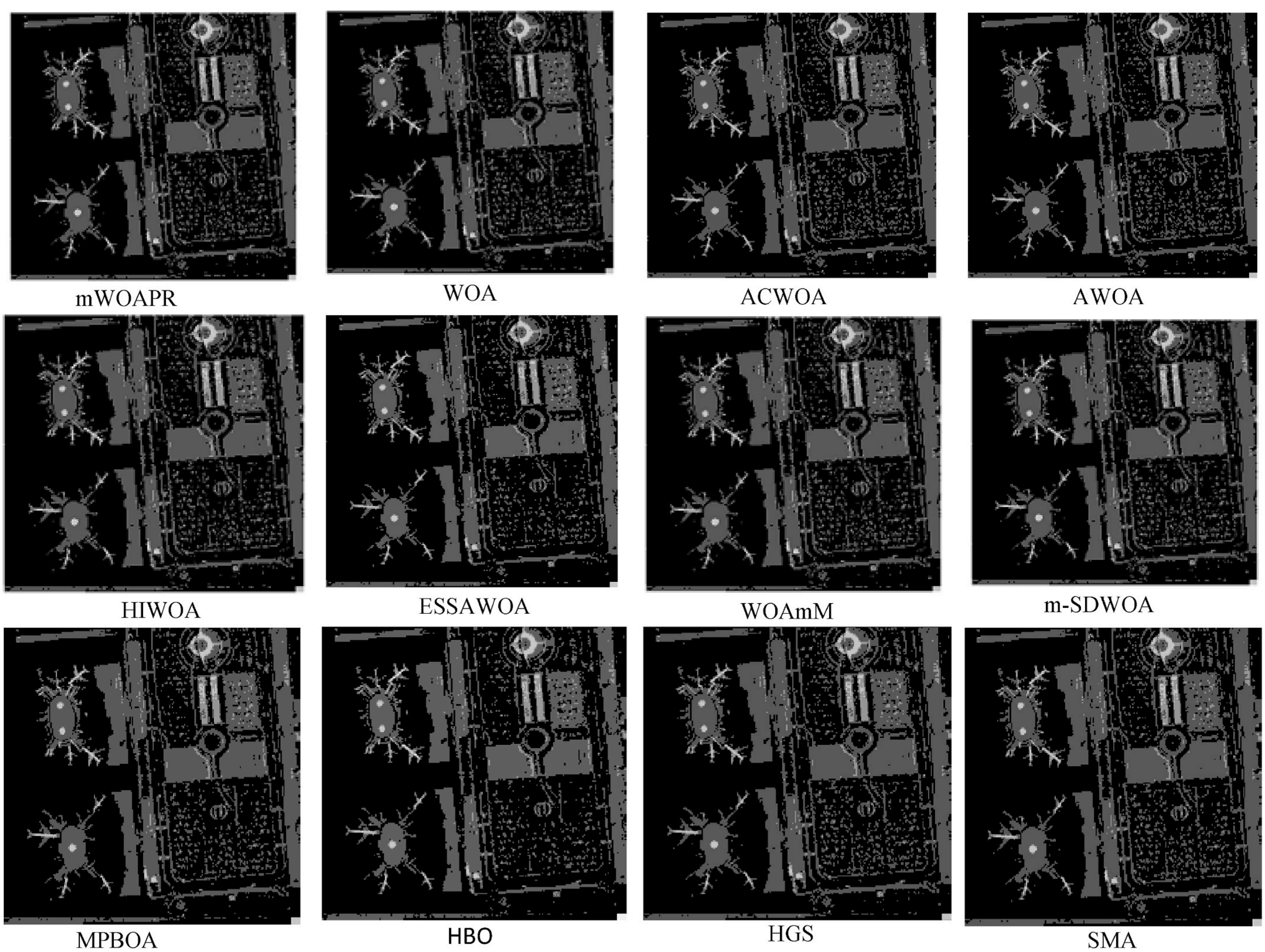

Fig. 3. Segmented images of image airport using Kapur's entropy at level 4.

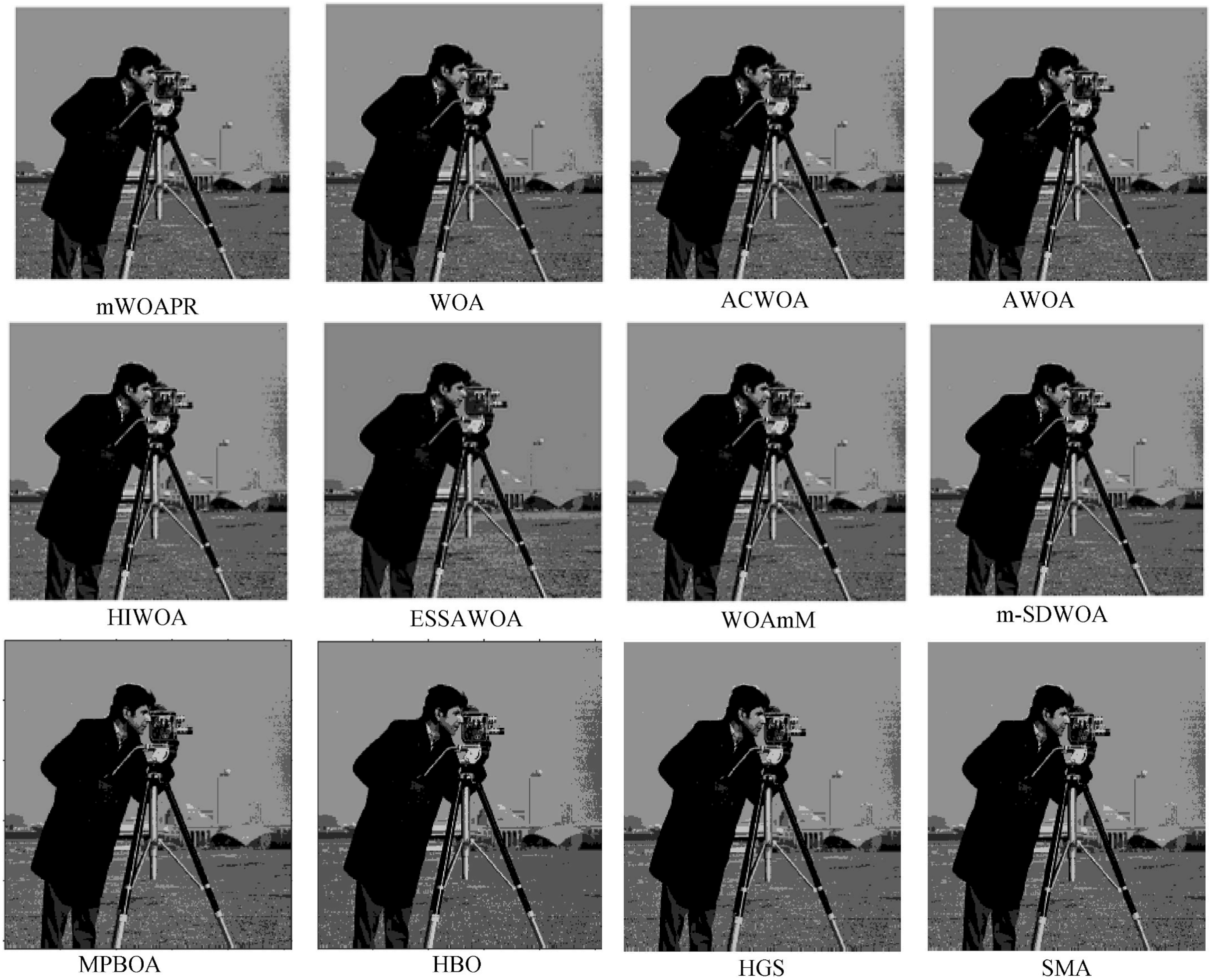

Fig. 4. Segmented images of image cameraman using Kapur's entropy at level 5.

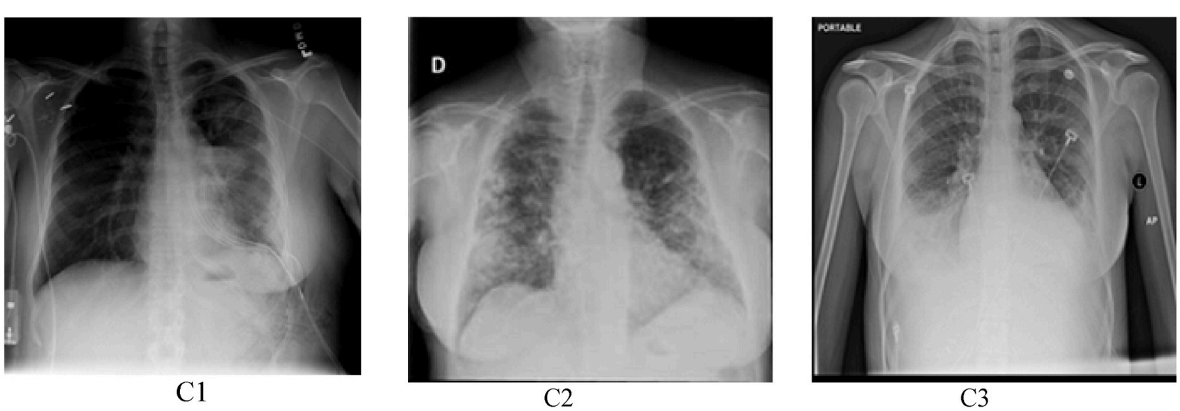

Fig. 5. COVID-19 X-ray images used for segmentation.

Table 8
Comparison of results using image C1.

Algorithm	Image	Level	Intensity	Mean	Std	PSNR	SSIM	Best
mWOAPR	C1	3	97 170 256	18.2830	1.4424e-14	14.9556	0.4004	18.2830
WOA			97 170 256	18.2830	3.6678e-05	14.9556	0.4004	18.2830
ACWOA			97 170 256	18.2824	6.4541e-04	14.9556	0.4004	18.2830
AWOA			97 170 256	18.2830	3.6678e-05	14.9556	0.4004	18.2830
HIWOA			97 170 256	18.2827	4.7091e-04	14.9556	0.3707	18.2830
ESSAWOA			95 171 253	18.2252	0.0825	14.0285	0.4039	18.2815
WOAmM			97 170 256	18.2830	3.6678e-05	14.9556	0.4004	18.2830
m-SDWOA			97 170 256	18.2829	8.1730e-05	14.9556	0.4004	18.2830
MPBOA			97 170 252	18.2821	0.0007	14.9556	0.4004	18.2830
HBO			98 181 253	18.0402	0.1601	14.5199	0.3978	18.2656
HGS			97 170 256	18.2827	0.0004	14.9556	0.4004	18.2830
SMA			97 170 256	18.2830	0.0000	14.9556	0.4004	18.2830
mWOAPR	C1	4	70 125 182 256	22.8257	0.0029	17.7907	0.5080	22.8263
WOA			70 125 182 256	22.8252	2.5645e-04	17.7907	0.5080	22.8263
ACWOA			70 125 182 254	22.8132	0.0111	17.7907	0.5080	22.8263
AWOA			70 125 182 256	22.8247	0.0040	17.7907	0.5080	22.8263
HIWOA			70 125 182 256	22.8128	0.0131	17.7907	0.5080	22.8263
ESSAWOA			70 128 182 255	22.7271	0.0891	17.8071	0.5081	22.8213
WOAmM			70 125 182 256	22.8238	0.0055	17.7907	0.5080	22.8263
m-SDWOA			70 125 182 256	22.8254	0.0030	17.7907	0.5080	22.8263
MPBOA			70 126 182 254	22.8212	0.0072	17.7929	0.5082	22.8262
HBO			56 112 181 249	22.4824	0.2043	17.8247	0.5339	22.7380
HGS			70 125 182 256	22.8181	0.0081	17.7907	0.5080	22.8263
SMA			70 125 182 256	22.8236	0.0060	17.7907	0.5080	22.8263
mWOAPR	C1	5	65 115 165 215 256	27.1895	0.0018	18.7213	0.5189	27.1904
WOA			65 115 165 215 256	27.1891	0.0023	18.7213	0.5189	27.1904
ACWOA			64 114 163 215 256	27.1549	0.0355	18.7616	0.5236	27.1895
AWOA			65 115 165 215 256	27.1881	0.0042	18.7213	0.5189	27.1904
HIWOA			63 114 165 215 253	27.1413	0.0598	18.7858	0.5147	27.1892
ESSAWOA			62 118 169 214 256	26.8709	0.2209	18.7067	0.5185	27.1621
WOAmM			65 115 165 215 256	27.1892	0.0015	18.7213	0.5189	27.1904
m-SDWOA			65 115 165 215 256	27.1889	0.0026	18.7213	0.5189	27.1904
MPBOA			64 114 164 215 252	27.1507	0.0325	18.7634	0.5224	27.1904
HBO			74 125 170 210 245	26.4360	0.3223	18.2756	0.4932	26.9687
HGS			65 115 165 215 256	27.1667	0.0204	18.7213	0.5189	27.1904
SMA			65 115 165 215 256	27.1893	0.0017	18.7213	0.5189	27.1904
mWOAPR	C1	6	54 94 133 174 215 256	31.2096	0.0039	20.4227	0.5700	31.2123
WOA			54 94 133 174 215 256	31.2074	0.0051	20.4227	0.5700	31.2123
ACWOA			54 96 138 178 215 253	31.1378	0.0905	20.3763	0.5682	31.2055
AWOA			54 93 133 173 215 253	31.2051	0.0058	20.4495	0.5705	31.2119
HIWOA			52 95 135 175 215 256	31.0939	0.0800	20.5033	0.5783	31.2035
ESSAWOA			54 88 131 175 214 253	30.5006	0.4470	20.4034	0.5699	31.1726
WOAmM			54 94 133 174 215 256	31.2086	0.0045	20.4227	0.5700	31.2123
m-SDWOA			54 94 133 174 215 256	31.2075	0.0055	20.4227	0.5700	31.2123
MPBOA			53 93 134 177 215 256	31.1589	0.0516	20.4145	0.5722	31.2076
HBO			60 95 126 159 202 253	30.0098	0.5681	20.3634	0.5712	30.9151
HGS			53 93 132 172 215 256	31.1118	0.1015	20.4911	0.5752	31.2105
SMA			54 94 133 174 215 255	31.1909	0.0674	20.4227	0.5700	31.2123

(PSNR) and structural similarity index measure (SSIM) to measure performance.

4.3.1. Peak signals to noise ratio (PSNR)

Degree of segmented image quality measured in decibels (DB) by PSNR. Mathematically, it can be written as,

$$PSNR = 10 \log_{10}\left(\frac{255^2}{MSE}\right) \tag{15}$$

where MSE represents the mean square error. MSE is evaluated as follows,

$$MSE = \frac{i}{MN}\sum_{i=1}^{M}\sum_{j=1}^{N}[I(i,j) - I'(i,j)]^2 \tag{16}$$

In Eqn. (16), the variables M and N are the sizes of the images. I and I' represents the original and segmented image individually.

4.3.2. Structural similarity index measure (SSIM)

SSIM is used to gauge the picture's structural uprightness, and it is another metric used for assessing performance. Expecting that I is the unsegmented picture and I' is the segmented picture, the primary similitude between them can be determined as follows

$$SSIM = \frac{(2\mu_I\mu_{I'} + c_1)(2\sigma_{I,I'} + c_2)}{(\mu_I^2 + \mu_{I'}^2 + C_1)(\sigma_I^2 + \sigma_{I'}^2 + C_2)} \tag{17}$$

In Eqn. (17), μ_I, $\mu_{I'}$ are the average greyscale of images I and I'. The variance of images I and I' is represented by σ_I^2 and $\sigma_{I'}^2$ respectively. $\sigma_{I,I'}$ is the covariance of the images I and I', constants c_1 and c_2 are used for maintaining the stability of the system.

5. Experimental results and analysis

The suggested method's performance is validated in this section by segmenting two sets of images using Kapur's entropy-based multilevel thresholding approach. The benchmark images are given in Fig. 2 together with their associated histogram. The COVID-19 X-ray images from the Kaggle data collection are the second. The evaluated outcomes are compared to the original metaheuristic algorithms and modified algorithms. The WOA is one of the basic metaheuristics used for comparison. The other fundamental algorithms are those that have lately

Table 9
Comparison of results using image C2.

Algorithm	Image	Level	Intensity	Mean	Std	PSNR	SSIM	Best
mWOAPR	C2	3	90 145 256	17.2245	4.0978e-05	16.6228	0.6226	17.2245
WOA			90 145 256	17.2245	4.1866e-05	16.6228	0.6226	17.2245
ACWOA			90 145 256	17.2235	0.0017	16.6228	0.6226	17.2245
AWOA			90 145 256	17.2242	7.5523e-04	16.6228	0.6213	17.2245
HIWOA			90 145 256	17.2233	0.0018	16.6228	0.6195	17.2245
ESSAWOA			91 146 249	17.2143	0.0156	16.6205	0.6201	17.2240
WOAmM			90 145 256	17.2245	1.1765e-14	16.6228	0.6226	17.2245
m-SDWOA			90 145 256	17.2245	1.7768e-05	16.6228	0.6226	17.2245
MPBOA			90 145 254	17.2239	0.0009	16.6228	0.6226	17.2245
HBO			90 146 250	17.1351	0.0818	16.6554	0.6206	17.2236
HGS			90 145 256	17.2244	0.0004	16.6228	0.6226	17.2245
SMA			90 145 256	17.2245	0.0000	16.6228	0.6226	17.2245
mWOAPR	C2	4	74 117 160 256	21.4175	0.0018	19.4197	0.6671	21.4182
WOA			74 117 160 256	21.4161	6.3623e-05	19.4197	0.6671	21.4182
ACWOA			74 117 160 256	21.4116	0.0124	19.4197	0.6671	21.4182
AWOA			74 117 160 256	21.4146	0.0068	19.4197	0.6587	21.4182
HIWOA			74 117 160 256	21.4108	0.0168	19.4197	0.6627	21.4182
ESSAWOA			72 115 160 219	21.2785	0.1491	19.4845	0.6685	21.4074
WOAmM			74 117 160 256	21.4175	0.0035	19.4197	0.6671	21.4182
m-SDWOA			74 117 160 256	21.4172	4.7195e-05	19.4197	0.6671	21.4182
MPBOA			73 117 160 256	21.4132	0.0032	19.4717	0.6679	21.4180
HBO			69 117, 164 240	21.1007	0.1652	19.6535	0.6600	21.3782
HGS			74 117 160 256	21.4098	0.0117	19.4197	0.6671	21.4182
SMA			74 117 160 256	21.4171	0.0002	19.4197	0.6671	21.4182
mWOAPR	C2	5	74 117 160 211 256	25.5571	0.0557	19.4291	0.6672	25.5731
WOA			74 117 160 211 256	25.5567	0.0218	19.4291	0.6672	25.5731
ACWOA			74 118 160 211 256	25.4913	0.0814	19.4465	0.6673	25.5719
AWOA			74 117 160 211 256	25.5352	0.0839	19.4291	0.6598	25.5731
HIWOA			74 117 160 211 256	25.4748	0.0773	19.4291	0.6617	25.5731
ESSAWOA			65 113 156 211 252	25.1423	0.2800	19.5578	0.6828	25.5338
WOAmM			74 117 160 211 256	25.5557	0.0068	19.4291	0.6672	25.5731
m-SDWOA			74 117 159 211 256	25.5365	0.0405	19.4038	0.6696	25.5728
MPBOA			54 92 129 164 256	25.2533	0.0055	21.6189	0.7184	25.2628
HBO			55 87 136 169 247	24.7263	0.2588	21.3398	0.6929	25.1413
HGS			72 117 160 211 256	25.4029	0.1459	19.5372	0.6689	25.5705
SMA			74 117 160 211 256	25.5361	0.1047	19.4291	0.6672	25.5731
mWOAPR	C2	6	6 60 99 149 242 256	29.3914	0.0738	19.0259	0.7189	29.5190
WOA			55 93 129 165 211 256	29.3677	0.0572	21.6542	0.7157	29.4173
ACWOA			5 55 102 156 209 256	29.3676	0.0926	19.3451	0.7067	29.5184
AWOA			5 57 102 160 256 256	29.3373	0.1309	19.2933	0.7021	29.5184
HIWOA			7 44 85 148 243 256	29.1854	0.2041	18.2031	0.7011	29.3950
ESSAWOA			6 64 110 149 256 256	28.8745	0.4247	19.2485	0.7231	29.5088
WOAmM			5 57 112 158 244 256	29.3763	0.0954	19.7313	0.7054	29.5789
m-SDWOA			7 58 108 145 226 256	29.3561	0.0703	18.8495	0.7308	29.4787
MPBOA			49 82 113 155 211 250	28.9858	0.1205	20.5749	0.7301	29.2399
HBO			34 69 98 156 212 255	28.3496	0.3083	19.5088	0.7163	29.0105
HGS			9 50 104 160 256 256	29.1273	0.2325	19.3374	0.7016	29.4210
SMA			5 56 100 151 249 256	29.4776	0.1141	19.1503	0.7156	29.5754

been published, including heap-based optimizer (HBO) [46], hunger games search (HGS) [47], and slime mould algorithm (SMA) [48]. Modified variants used for the comparison are A-C parametric whale optimization algorithm (ACWOA) [49], adaptive whale optimization algorithm (AWOA) [50], hybrid improved whale optimization algorithm (HIWOA) [51], enhanced Whale optimization algorithm integrated with salp swarm algorithm (ESSAWOA) [52], Whale optimization algorithm with modified mutualism (WOAmM) [33], Modified whale optimization algorithm hybridized with DE and SOS (m-SDWOA) [53], and Butterfly optimization algorithm modified with mutualism and parasitism (MPBOA) [54]. The advantages and disadvantages of the algorithms employed for comparison are given in subsection 5.1. Among these methods, HBO, HGS, and SMA are the very recently published algorithms. ACWOA, AWOA, HIWOA, ESSAWOA, WOAmM, and m-SDWOA are the recently published WOA variants. WOA is the component algorithm of mWOAPR. All the algorithms mentioned proved their ability to solve numerous optimization issues. MPBOA is a recently published method that has solved the image segmentation problem with greater efficacy. The parameters of all the algorithms used for assessment are set as suggested in the respective study. The termination condition for all algorithms is 5000 function evaluations. A fixed population of size 50 is used during evaluation. The mean, standard deviation, and best values for each image are calculated from 30 independent runs at various threshold levels, given the best values of image quality measuring matrices, such as PSNR and SSIM. All the experiments have been executed on MATLAB R2015a on a Windows 2010 PC with an Intel Core i3 processor and 8 GB RAM.

5.1. Advantage and disadvantages of the compared algorithms

Every technique has some advantages and disadvantages, and thus the algorithms considered in this study for comparison have certain advantages and disadvantages. In this subsection, we mention the advantages and disadvantages of the employed methods.

WOA can be implemented quickly and require only a few parameters to fine-tune. But the algorithm has a slow convergence rate and is easily stuck into local solutions [55]. In HBO, high exploration ability while early iterations, the emergence of exploitation ability, and balance between the global and local search are implemented [46]. Still, the algorithm stuck into local solutions [56]. The algorithm HGS was proposed with a simple structure, executed with a unique stability feature [47]. HGS employs several parameters. In runtime, HGS may take a longer time to search the

Table 10
Comparison of results using image C3.

Algorithm	Image	Level	Intensity	Mean	Std	PSNR	SSIM	Best
mWOAPR	C3	3	88 157 256	18.2020	7.2416e-14	15.0644	0.5109	18.2020
WOA			88 157 256	18.2020	3.6134e-13	15.0644	0.5109	18.2020
ACWOA			88 157 256	18.2019	6.3185e-04	15.0644	0.5109	18.2020
AWOA			88 157 256	18.2020	7.8476e-14	15.0644	0.5103	18.2020
HIWOA			88 157 256	18.2019	8.9770e-04	15.0644	0.5049	18.2020
ESSAWOA			88 157 252	18.1918	0.0277	15.0644	0.5109	18.2020
WOAmM			88 157 256	18.2020	3.6134e-13	15.0644	0.5109	18.2020
m-SDWOA			88 157 256	18.2020	3.6134e-13	15.0644	0.5109	18.2020
MPBOA			88 157 254	18.2018	0.0004	15.0644	0.5109	18.2020
HBO			93 159 255	18.0726	0.1048	14.7865	0.4993	18.1970
HGS			88 157 256	18.2020	0.0001	15.0644	0.5109	18.2020
SMA			88 157 256	18.2020	0.0000	15.0644	0.5109	18.2020
mWOAPR	C3	4	72 123 174 256	22.6489	9.3530e-05	18.4500	0.6078	22.6489
WOA			72 123 174 256	22.6489	1.2746e-04	18.4500	0.6078	22.6489
ACWOA			72 123 174 256	22.6473	0.0036	18.4500	0.6078	22.6489
AWOA			72 123 174 256	22.6488	1.3974e-04	18.4500	0.6026	22.6489
HIWOA			72 123 174 256	22.6486	5.8876e-04	18.4500	0.6022	22.6489
ESSAWOA			70 122 173 243	22.5534	0.0985	18.5492	0.6144	22.6461
WOAmM			72 123 174 256	22.6488	1.6908e-04	18.4500	0.6078	22.6489
m-SDWOA			72 123 174 256	22.6489	1.1249e-04	18.4500	0.6078	22.6489
MPBOA			72 123 174 254	22.6470	0.0012	18.4500	0.6078	22.6489
HBO			75 136 175 250	22.2993	0.2131	17.7758	0.5784	22.5725
HGS			72 123 174 256	22.6440	0.0110	18.4500	0.6078	22.6489
SMA			72 123 174 256	22.6488	0.0002	18.4500	0.6078	22.6489
mWOAPR	C3	5	66 107 147 186 256	26.6937	2.6062e-04	20.3347	0.6597	26.6939
WOA			66 107 147 186 256	26.6937	2.6807e-04	20.3347	0.6597	26.6939
ACWOA			66 107 147 186 253	26.6871	0.0122	20.3347	0.6597	26.6939
AWOA			66 107 147 186 256	26.6934	7.2364e-04	20.3347	0.6573	26.6939
HIWOA			66 107 147 186 251	26.6821	0.0458	20.3347	0.6520	26.6939
ESSAWOA			71 111 147 188 256	26.3930	0.1612	20.0415	0.6456	26.6705
WOAmM			66 107 147 186 256	26.6936	4.2296e-04	20.3347	0.6597	26.6939
m-SDWOA			66 107 147 186 256	26.6935	6.3076e-04	20.3347	0.6597	26.6939
MPBOA			66 107 147 186 247	26.6886	0.0038	20.3347	0.6597	26.6939
HBO			57 103 148 188 238	26.2281	0.2509	20.2647	0.6630	26.6309
HGS			67 108 147 186 256	26.6535	0.0627	20.3148	0.6579	26.6932
SMA			66 107 147 186 256	26.6930	0.0012	20.3347	0.6597	26.6939
mWOAPR	C3	6	64 104 143 182 221 256	30.4888	0.0031	20.5418	0.6639	30.4935
WOA			67 108 147 186 242 256	30.4879	0.0051	20.3148	0.6579	30.5006
ACWOA			68 107 149 189 242 256	30.4701	0.0395	20.1720	0.6505	30.4930
AWOA			66 106 147 186 242 256	30.4784	0.0442	20.3105	0.6621	30.5000
HIWOA			34 69 109 149 187 252	30.4106	0.0965	20.4647	0.6592	30.4868
ESSAWOA			63 99 143 183 222 250	30.0777	0.3081	20.4117	0.6624	30.4686
WOAmM			64 104 143 181 221 256	30.4879	0.0038	20.5315	0.6643	30.4932
m-SDWOA			66 107 149 188 242 256	30.4881	0.0042	20.2753	0.6546	30.4930
MPBOA			63 105 141 178 217 255	30.4701	0.0157	20.6468	0.6642	30.4853
HBO			40 82 119 153 194 248	29.8208	0.2780	21.5414	0.6965	30.3395
HGS			63 107 144 181 217 256	30.4259	0.0542	20.6511	0.6611	30.4815
SMA			64 104 143 181 221 252	30.4575	0.0560	20.5315	0.6643	30.4936

Table 11
Algorithms with maximum mean fitness in different levels of COVID-19 X-ray images.

Image	Level	Algorithm
C1	3	mWOAPR, WOA, AWOA, WOAmM, SMA
	4	mWOAPR
	5	mWOAPR
	6	mWOAPR
C2	3	mWOAPR, WOA, WOAmM, m-SDWOA, SMA
	4	mWOAPR, WOAmM
	5	mWOAPR
	6	mWOAPR
C3	3	mWOAPR, WOA, AWOA, WOAmM, m-SDWOA, HGS, SMA
	4	mWOAPR, WOA, m-SDWOA
	5	mWOAPR, WOA
	6	mWOAPR

region effectively. SMA guarantees the act of explorations while accomplishing exploitations; this balances the algorithm's global and local search [48]. But the algorithm is often trapped in local solutions while solving continuous global optimization issues [57]. In ACWOA and AWOA of parameters, exploration and exploitation ability of the algorithms increased modifying parameters of WOA. Despite modifications performance of the algorithms while solving high dimensional problems is not satisfactory. HIWOA has a higher exploration ability than WOA; it diminishes the chance of the algorithm being trapped into the local solution [51]. However, the introduction of a feedback mechanism in HIWOA increases the complexity of the algorithm. ESSAWOA has increased exploration and exploitation ability than WOA by introducing the strategies like SSA and LOBL, which enlarged the computational cost of the algorithm. In WOAmM, m-SDWOA, and MPBOA, the exploration and exploitation ability of the algorithms were balanced by amplifying the diversity of the algorithms. However, the computational complexity of these algorithms was increased with the modification.

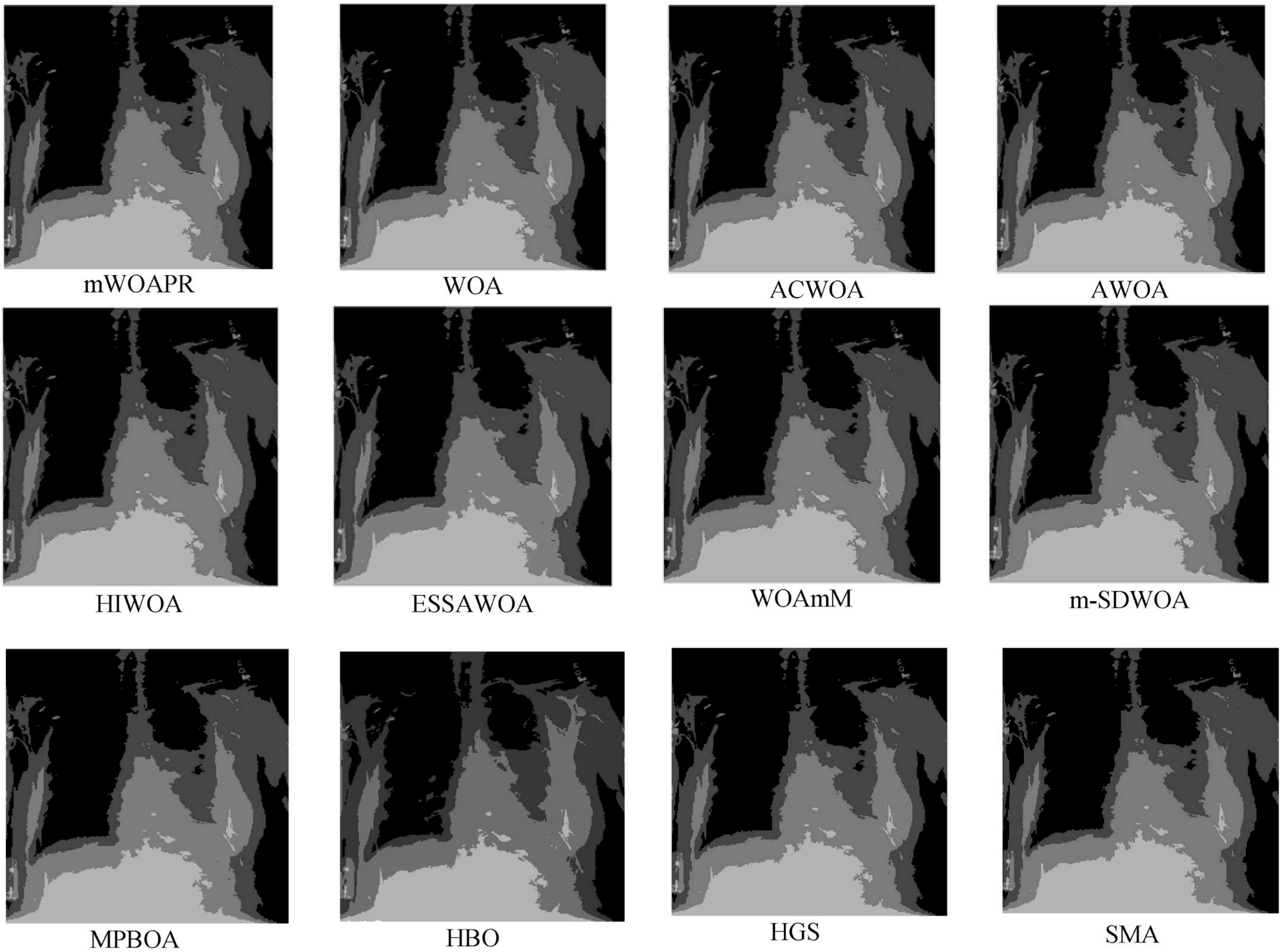

Fig. 6. Segmented images of COVID-19 X-ray image1 (C1) using Kapur's entropy at level 4.

5.2. Analysis of experimental results on benchmark images

The threshold levels 3, 4, 5, and 6 are used to evaluate the test images in Fig. 2. Tables 1–6 provide the mean, standard deviation (std), and the optimum value of image quality matrices. Columns 5, 6, and 9 represent the mean, standard deviation, and best fitness value, respectively. Columns 7 and 8 of the tables contain the optimum PSNR and SSIM values. Table 1 depicts that the algorithms mWOAPR, WOAmM, m-SDWOA, and SMA evaluate similar fitness at threshold level 3. SMA has the smallest standard deviation of all the models. The fitness values achieved by mWOAPR at threshold levels 4, 5, and 6 are superior to those obtained by the other algorithms. In Table 2, at threshold level 3, mWOAPR, AWOA, WOAmM, m-SDWOA, and SMA acquire similar optimal results. However, the standard deviation value obtained by mWOAPR, m-SDWOA, and SMA is equal. At threshold level 4, mWOAPR and SMA achieve the same optimal value, and mWOAPR's standard deviation is the lowest of all. The assessed optimal values of mWOAPR are maximum than the comparable algorithms for threshold levels 5 and 6. Table 3 shows that at threshold level 3, mWOAPR, m-SDWOA, and SMA all achieve the same optimal value, with SMA's standard deviation being the lowest of all. mWOAPR can locate the highest optimal outcome at threshold levels 4, 5, and 6. Table 4 shows the maximum and equal optimal values calculated by mWOAPR and MPBOA at level 3; the standard deviation value calculated by MPBOA is the smallest. Compared to the employed algorithms, the fitness outcomes of mWOAPR are best at threshold levels 4, 5, and 6. Table 5 shows that WOA, AWOA, WOAmM, m-SDWOA, SMA, and mWOAPR calculate the same optimal fitness at threshold level 3. At this threshold level, the estimated standard deviation value of SMA is the lowest of all the algorithms. mWOAPR analyses maximal optimal fitness at threshold levels 4 and 6. The evaluated optimal fitness of mWOAPR and m-SDWOA are similar at threshold level 5 and the maximum. Among all the algorithms used in this experiment, the proposed technique had the lowest standard deviation. Table 6 shows that WOA, AWOA, WOAmM, m-SDWOA, SMA, and mWOAPR all have the same optimal fitness at threshold level 3. At this threshold level, SMA has the lowest estimated standard deviation value among the algorithms. mWOAPR determines the greatest optimal fitness among the compared algorithms at threshold levels 4, 5, and 6. Table 7 shows the algorithms achieved the highest mean fitness in the benchmark images used in the study with various threshold settings. Fig. 3 and Fig. 4 show segmented images from several algorithms using images of an airport and a cameraman at threshold levels 4 and 5. After comparing the findings of all of the tables, it can be determined that at threshold level 3, the majority of the algorithms evaluate optimal fitness in the same way. At threshold level 3, SMA emerges as the algorithm with the lowest standard deviation. At image airport threshold levels 3 and 4, MPBOA, HBO, HGS, and SMA have higher PSNR values than mWOAPR. The efficacy of mWOAPR improves as the threshold level is raised. mWOAPR maintains the leading place in most threshold levels throughout all test images evaluating estimated maximum optimal fitness.

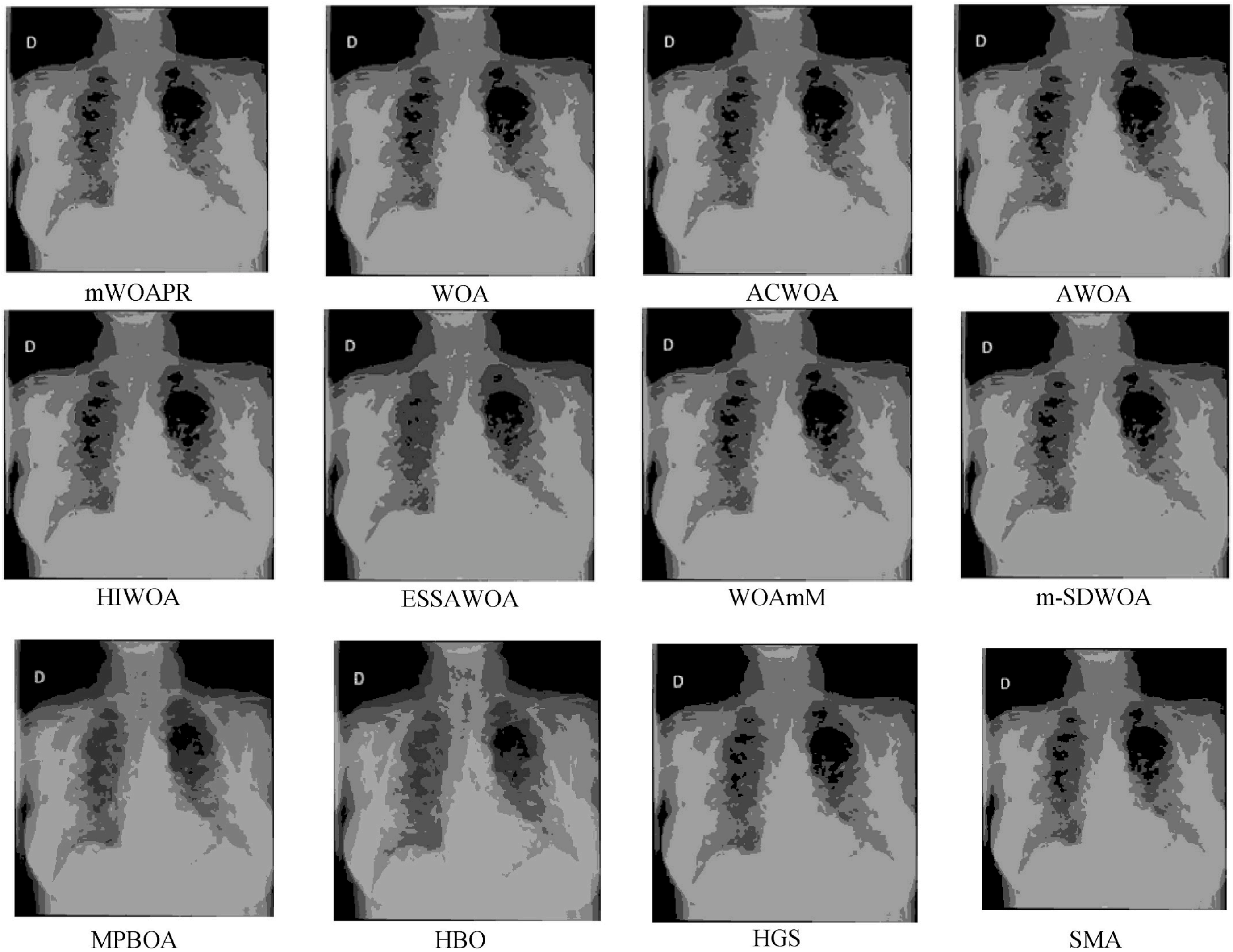

Fig. 7. Segmented images COVID-19 X-ray image 2 (C2) using Kapur's entropy at level 5.

5.3. Analysis of experimental results on COVID-19 chest X-ray images

The threshold levels 3, 4, 5, and 6 are used to evaluate the test images in Fig. 5. Tables 8–10 provide the mean, standard deviation (std), and outcomes of image quality matrices. Columns 5, 6, and 9 represent the mean, standard deviation, and best fitness values, respectively. Columns 7 and 8 of the tables show the best PSNR and SSIM values. In Table 8, at threshold level 3, the algorithms mWOAPR, WOA, AWOA, WOAmM, and SMA evaluate equal fitness; the standard deviation value of SMA is minimum than the others. The proposed mWOAPR estimates the second lowest standard deviation value after SMA. The fitness values obtained by mWOAPR are the highest of the other algorithms for threshold levels 4, 5, and 6. In Table 9, the optimum values for mWOAPR, WOA, WOAmM, m-SDWOA, and SMA are identical at threshold level 3. Among the comparison algorithms, SMA obtains the lowest standard value. At threshold level 4, mWOAPR and WOAmM have the same optimal value, although mWOAPR has a lower standard deviation than WOAmM. The assessed optimal values of mWOAPR are the highest of all the comparison algorithms for threshold levels 5 and 6. Table 10 shows that at threshold level 3, mWOAPR, WOA, AWOA, WOAmM, m-SDWOA, HGS, and SMA all achieve the same optimal value, with SMA's standard deviation being the lowest. WOA and m-SDWOA provide comparable results as mWOAPR at threshold level 4. When compared to WOA, the evaluated standard value for mWOAPR is the smallest. WOA and mWOAPR are able to discover the maximum optimal outcome at threshold levels 5 and 6. The standard value determined by mWOAPR, on the other hand, is the bare minimum. mWOAPR's optimal fitness, as measured by threshold level 6, is the best of all the compared algorithms. The algorithms that achieved the highest mean fitness in different threshold levels of the COVID-19 X-ray images examined in this work are shown in Table 11. Segmented images of all the algorithms for image C1 at threshold level 4, C2 at threshold level 5, and C3 at threshold level 6 are given in Fig. 6, Fig. 7, and Fig. 8, respectively.

Based on the preceding explanation, mWOAPR is the best method for segmenting COVID-19 chest X-ray pictures among the compared algorithms. With increasing threshold levels, mWOAPR's segmentation performance improves.

5.4. Description of the lesion parts in COVID-19 X-ray images and comparison with normal chest X-ray image

Images (a), (b), and (c) in Fig. 9 exhibit COVID-19 X-ray images (C1, C2, C3) segmented by mWOAPR using thresholds 4, 5, and 6. The damaged area in each picture is the grey-colored portion indicated by a red arrow. The black area, indicated by the green arrow, is the unaffected segment. The COVID-19 X-ray images are divided, making it simple to identify the infected area and severity. It is clear from images (a), (b), and (c) in the given figure that image (c) has the highest

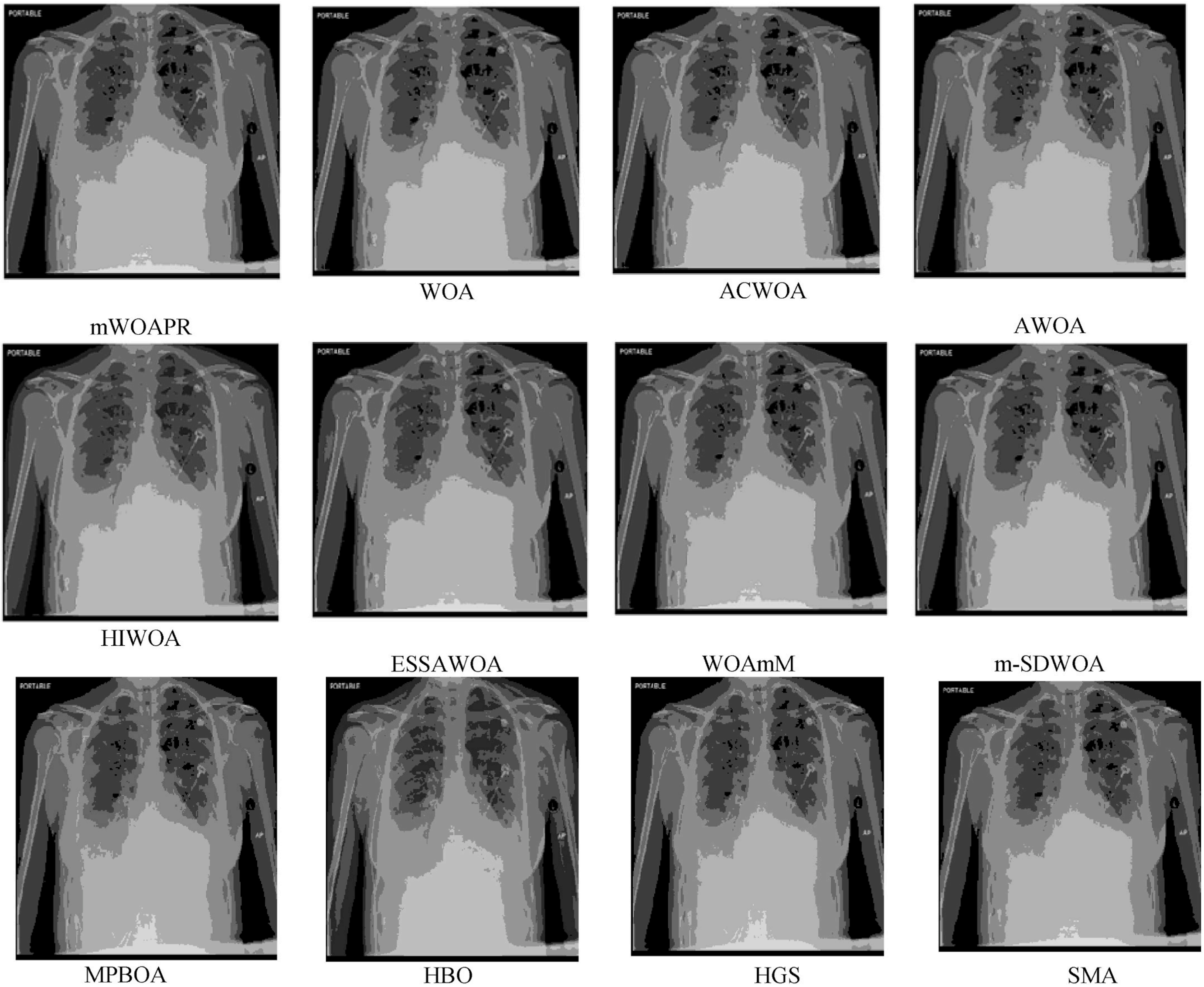

Fig. 8. Segmented images COVID-19 X-ray image 3 (C3) using Kapur's entropy at level 6.

infection. Even though the original X-ray images C2 and C3 are nearly identical, the segmented image reveals a greater disease effect in image C3.

The segmented image of a normal chest scan is shown in the image (d) in the figure. The vital organs, namely the lung and heart, are located in the upper abdomen areas colored green in the image (d). The black region confirms the patient's normalcy within the designated portion of the image. It is clear from the segmented images that image (d) has more active parts than other images in the figure.

6. Computational complexity analysis and statistical analysis

Here, the first subsection represents the worst-case runtime required for the algorithm to run. Here the computational complexity of mWOAPR is compared with WOA. In the second subsection, statistical analysis of the evaluated results is performed to check the proposed algorithm's performance statistically.

6.1. Analysis of computational complexity

The run time of an algorithm is directly related to the computational complexity of the algorithm. Here, in this section, the computational complexity of the algorithms WOA is evaluated to compare it with mWOAPR. Let *maxiter* is the maximum number of iterations used as termination criteria for both the algorithms.

6.1.1. Comparison of computational complexity with WOA

The primary strategies related to the computational complexity in WOA are:

(i) Initializing the whale population is $O(N)$, where N is the size of the population.
(ii) Fitness evaluation of initial population is $O(N)$.
(iii) Sorting the population and determining the best solution is $O(N^2)$.
(iv) While iteration, updating whale population, and evaluating fitness $O(2N)$.

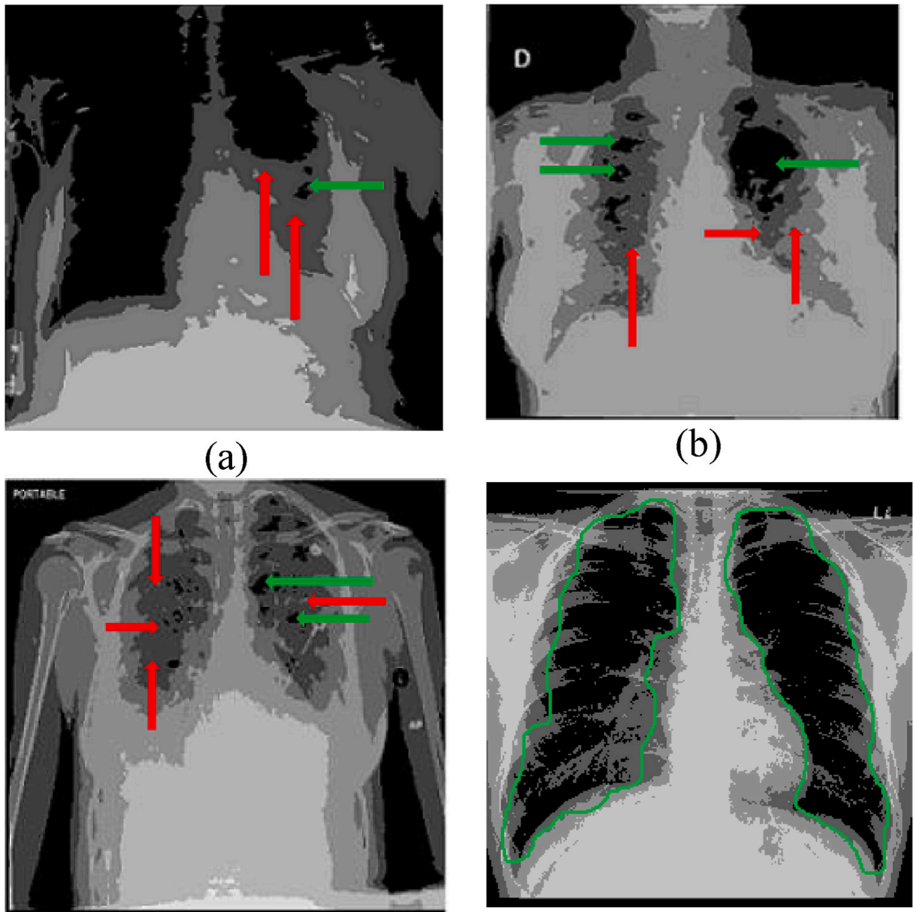

Fig. 9. Illustration of the lesion part and unaffected part in COVID-19 and normal X-ray image.

(v) While iteration, sorting the population and determining the best solution $O(N^2)$.

Therefore, the total time complexity of WOA is:

$$O(2N) + O(N^2) + maxiter\left(O(2N) + O(N^2)\right) == (max\_iter + 1)\left(O(N^2 + 2N)\right)$$

Though WOA and mWOAPR start with population N in mWOAPR, with increasing iteration, the population decreases gradually, and lastly, the value of population becomes 15 instead of N. Therefore, it is evident from the discussion that the complexity of mWOAPR is much lesser than that of WOA.

Table 12
Statistical comparison outcomes of the employed algorithms.

Algorithm	Mean rank	Final Rank	P-value
mWOAPR	11.18	1	P-value 4.28E-65 < 0.01 indicates that the hypothesis is rejected at 1% significance level. It implies that there is a significant difference in the performance of different algorithms.
WOA	9	5	
ACWOA	4.99	8	
AWOA	8.07	6	
HIWOA	3.89	10	
ESSAWOA	2	11	
WOAmM	9.39	2	
m-SDWOA	9.21	4	
MPBOA	4.94	9	
HBO	1	12	
HGS	5.04	7	
SMA	9.29	3	

6.2. Statistical analysis

Friedman test is employed for statistical comparison. Friedman's test is a nonparametric test used to find differences in treatments (methods) across multiple attempts (functions). It is used in place of the ANOVA test when the fundamental assumption of ANOVA is violated, i.e., data does not come from a normal population. This test extends the 'Paired samples Wilcoxon signed-rank test when there are more than three treatments (strategies). In the case of two treatments (strategies), both the tests are identical.

Table 12 depicts the result of Friedman's rank test. Column 2 of the table shows the mean rank of the algorithms used for comparison. In

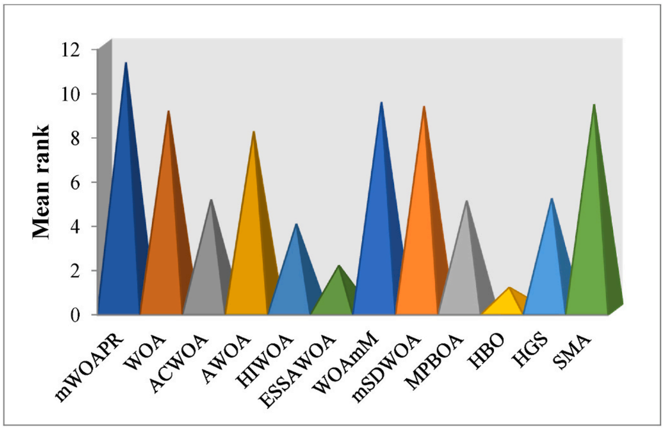

Fig. 10. Graphical representation of the evaluated mean rank.

column 3, the final position is calculated from the evaluated mean rank. The evaluated fitness values in threshold levels 3, 4, 5, and 6 of every algorithm's images are utilized to calculate the mean rank. Image segmentation is a maximization problem; hence, the algorithm with the highest mean rank is considered the best algorithm. The final rank of the other compared algorithms is determined using a similar process. Fig. 10 shows the graphical representation of the mean rank evaluated by Friedman's test.

6.3. Convergence analysis

Convergence graphs are mainly drawn to verify the solution generating speed of the algorithms. Figs. 11 and 12 show the convergence graphs drawn using the benchmark images and COVID-19 X-ray images. A population size of 50 and 5000 function evaluations is used as the end criteria to draw the graphs. In both, the figure graphs drawn in threshold levels 4, 5, and 6 are shown in row1, row2, and row 3, respectively. In every diagram, the function evaluation numbers are shown on the X-axis. The Y-axis represents the fitness values evaluated by the algorithms

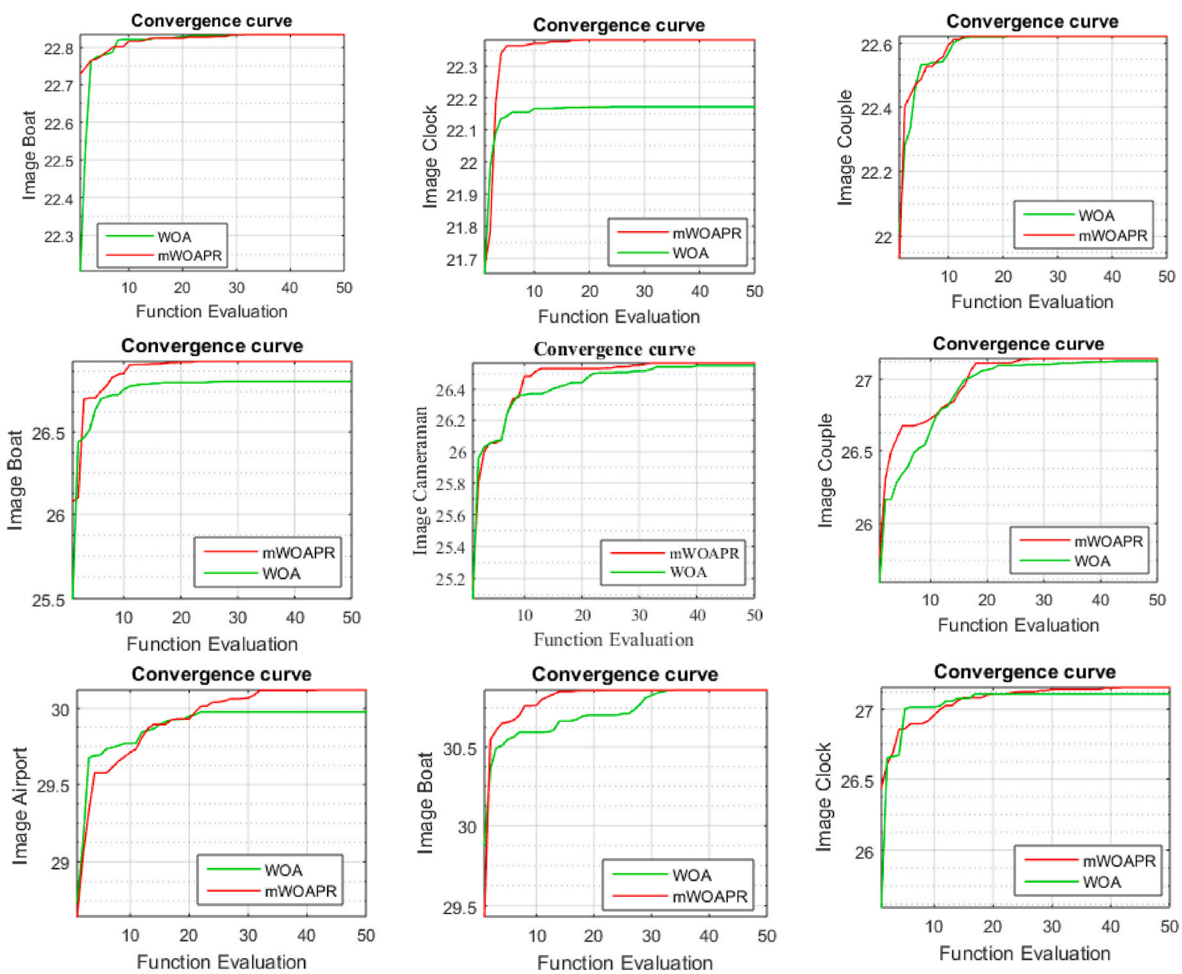

Fig. 11. Convergence curves of WOA and mWOAPR on benchmark images.

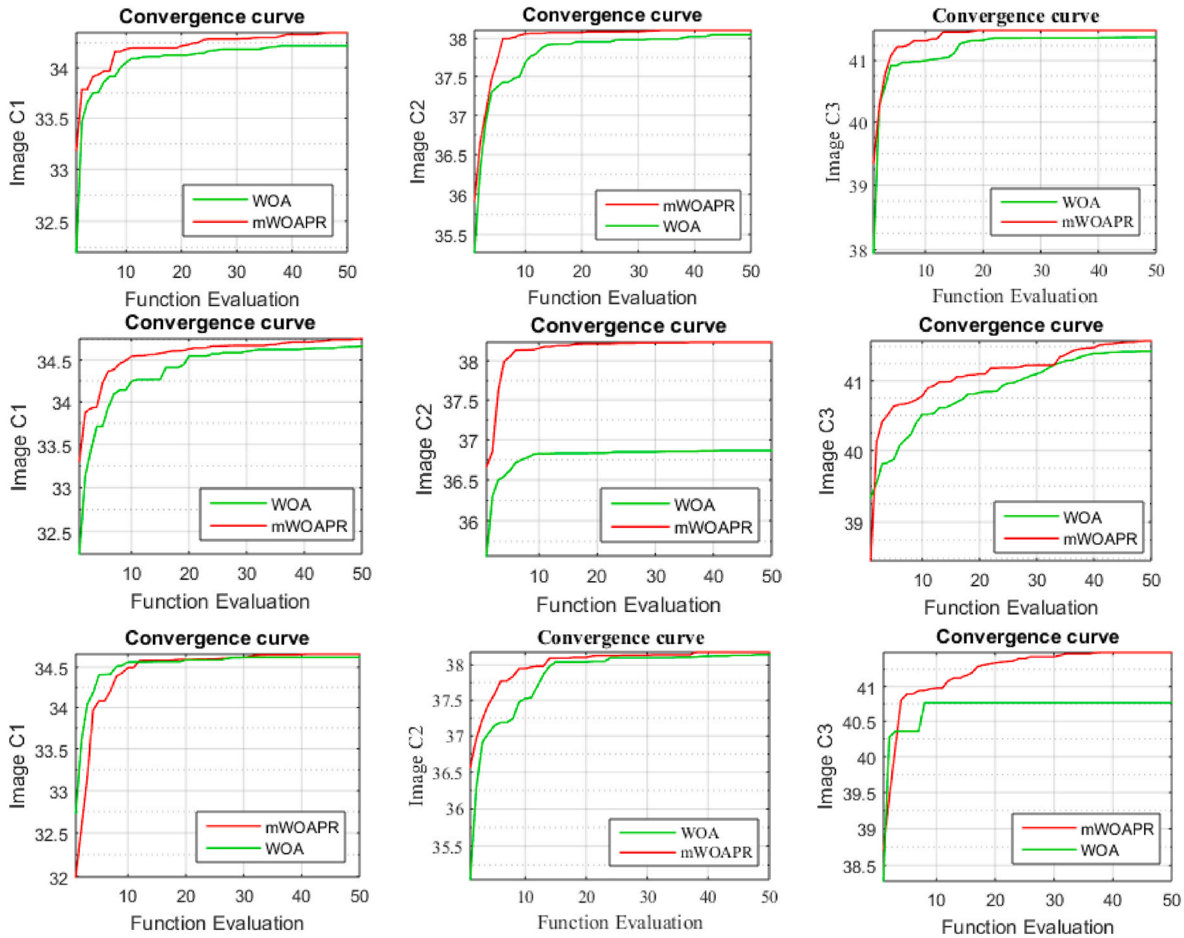

Fig. 12. Convergence curves of WOA and mWOAPR on COVID-19 X-ray images.

according to the function evaluation. The best value generated by an algorithm after every iteration is plotted until the termination criterion is satisfied. Among all the lines generated by the algorithms used for comparison, the line that touches the horizontal boundary first and its corresponding algorithm is considered faster convergence than the others. Similarly, the curve w.r.t. to the Y-axis shows the highest evaluated optimal value during convergence. The algorithm for which a curve touches the horizontal boundary faster and attains the highest optimal value on Y-axis is considered more efficient. Convergence curves of images including all the algorithms employed in the study using threshold 4, 5, and 6 are given in Fig. 1, Fig. 2 and Fig. 3 of Appendix-I.

7. Conclusion

This research introduces a new WOA version that improves the balance of the search processes. Basic, the search prey phase in basic WOA is eliminated by randomly initializing the solution during the exploration phase. The coefficient vector A and constant b parameter values are changed to aid exploration and exploitation processes. To increase convergence speed and exploitation, the population reduction method is used. During execution, a traversal parameter is introduced to pick the exploration or exploitation phase. The overall setup considerably improves the basic WOA's performance. The proposed method is used to separate benchmark images and COVID-19 X-ray images into two pieces, which may aid clinicians in identifying and planning treatment. The advantage of the projected mWOAPR algorithm over the comparative methods is confirmed by comparing the evaluated outcomes with several metaheuristic algorithms.

Declaration of interests

The authors declare that they have no known competing financial interests or personal relationships that could have appeared to influence the work reported in this paper.

Acknowledgment

The authors are extremely thankful to Dr. Saikat Kar, Department of Obstetrics and Gynecology, Agartala Government Medical College, Tripura, India, who helped to analyze the segmented COVID-19 images. The authors are also grateful to the editor and the reviewer for their valuable suggestions and comments, which helped improve the manuscript.

Appendix-I

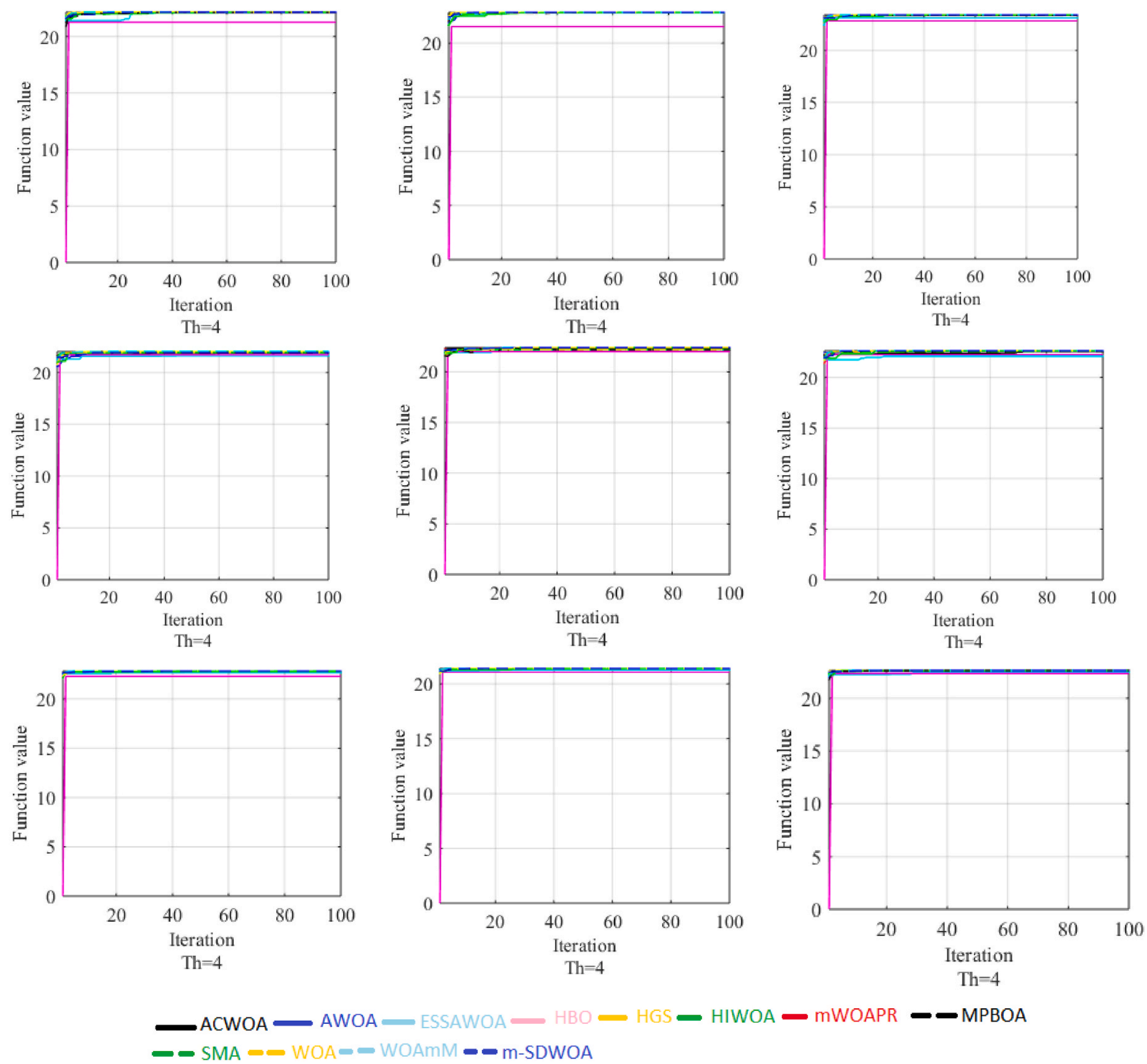

Fig. 1. Convergence curves of benchmark images a-f and Covid-19 X-Ray images using threshold-4.

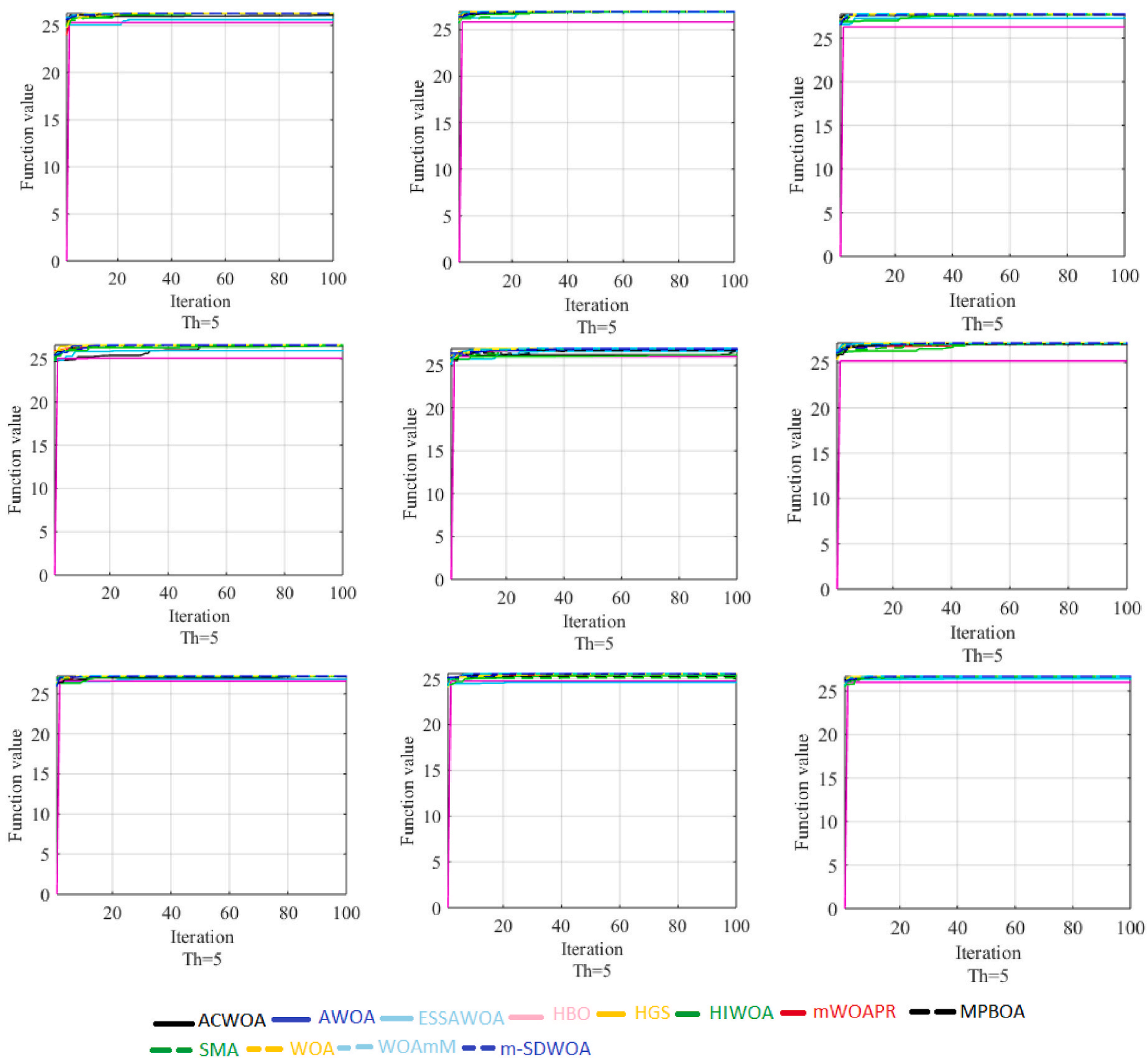

Fig. 2. Convergence curves of benchmark images a-f and Covid-19 X-Ray images using threshold-5.

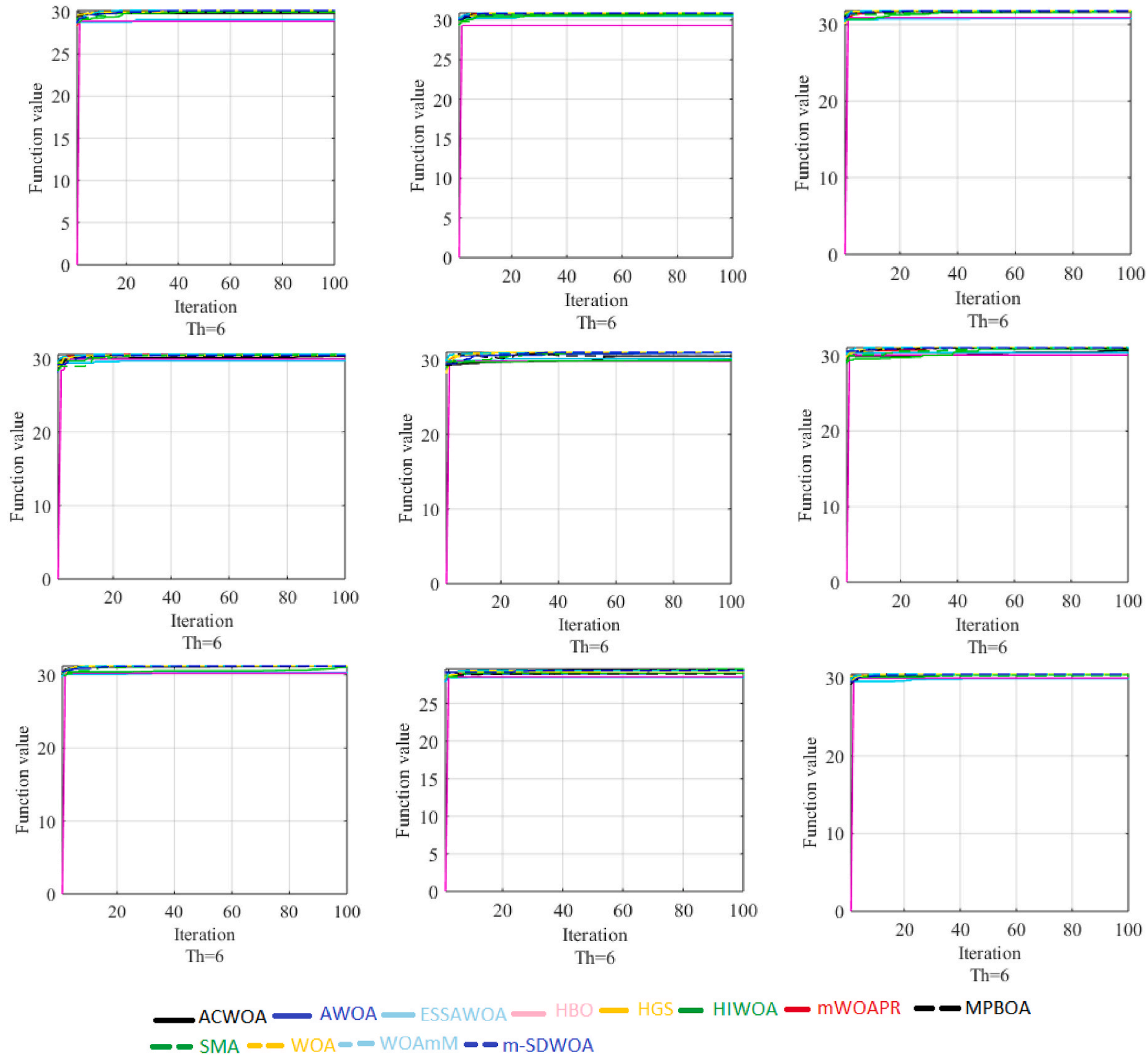

Fig. 3. Convergence curves of benchmark images a-f and Covid-19 X-Ray images using threshold-6.

References

[1] S.K. Sinha, A. Shakya, S.K. Prasad, S. Singh, N.S. Gurav, R.S. Prasad, S.S. Gurav, An in-silico evaluation of different Saikosaponins for their potency against SARS-CoV-2 using NSP15 and fusion spike glycoprotein as targets, J. Biomol. Struct. Dyn. 39 (9) (2021) 3244–3255, https://doi.org/10.1080/07391102.2020.1762741.

[2] S. Kumar, P.P. Sharma, U. Shankar, D. Kumar, S.K. Joshi, L. Pena, B. Rathi, Discovery of new hydroxyethylamine analogs against 3CLpro protein target of SARS-CoV-2: molecular docking, molecular dynamics simulation, and structure–activity relationship studies, J. Chem. Inf. Model. 60 (12) (2020) 5754–5770, https://doi.org/10.1021/acs.jcim.0c00326.

[3] G. Li, E. De Clercq, Therapeutic options for the 2019 novel coronavirus (2019-nCoV), Nat. Rev. Drug Discov. 19 (3) (2020) 149–150, https://doi.org/10.1038/d41573-020-00016-0.

[4] M. Yüce, E. Filiztekin, K.G. Özkaya, COVID-19 diagnosis—a review of current methods, Biosens. Bioelectron. (2020) 112752, https://doi.org/10.1016/j.bios.2020.112752.

[5] N. Taleghani, F. Taghipour, Diagnosis of COVID-19 for controlling the pandemic: a review of the state-of-the-art, Biosens. Bioelectron. (2020) 112830, https://doi.org/10.1016/j.bios.2020.112830.

[6] W.J. Guan, Z.Y. Ni, Y. Hu, W.H. Liang, C.Q. Ou, J.X. He, N.S. Zhong, China medical treatment expert group for Covid-19, Clinical characteristics of coronavirus disease 382 (18) (2019) 1708–1720, https://doi.org/10.1056/NEJMoa2002032, 1708-1720.

[7] S. Zhou, Y. Wang, T. Zhu, L. Xia, CT features of coronavirus disease 2019 (COVID-19) pneumonia in 62 patients in Wuhan, China, Am. J. Roentgenol. 214 (6) (2020) 1287–1294, https://doi.org/10.2214/AJR.20.22975.

[8] M. Chung, A. Bernheim, X. Mei, N. Zhang, M. Huang, X. Zeng, H. Shan, CT imaging features of 2019 novel coronavirus (2019-nCoV), Radiology 295 (1) (2020) 202–207, https://doi.org/10.1148/radiol.2020200230.

[9] A. Jacobi, M. Chung, A. Bernheim, C. Eber, Portable chest X-ray in coronavirus disease-19 (COVID-19): a pictorial review, Clin. Imag. 64 (2020) 35–42, https://doi.org/10.1016/j.clinimag.2020.04.001.

[10] C. Jin, W. Chen, Y. Cao, Z. Xu, Z. Tan, X. Zhang, J. Feng, Development and evaluation of an artificial intelligence system for COVID-19 diagnosis, Nat. Commun. 11 (1) (2020) 1–14, https://doi.org/10.1038/s41467-020-18685-1.

[11] J. Chen, K.C. See, Artificial intelligence for COVID-19: rapid review, J. Med. Internet Res. 22 (10) (2020), e21476, https://doi.org/10.2196/21476.

[12] L. Liu, D. Zhao, F. Yu, A.A. Heidari, C. Li, J. Ouyang, J. Pan, Ant colony optimization with Cauchy and greedy Levy mutations for multilevel COVID 19 X-ray image segmentation, Comput. Biol. Med. (2021), https://doi.org/10.1016/j.compbiomed.2021.104609, 104609.

[13] A. Sarkar, J. Vandenhirtz, J. Nagy, D. Bacsa, M. Riley, Identification of images of COVID-19 from chest X-rays using deep learning: comparing COGNEX VisionPro deep learning 1.0™ software with open source convolutional neural networks, SN Computer Science 2 (3) (2021) 1–16, https://doi.org/10.1007/s42979-021-00496-w.

[14] K. El Asnaoui, Y. Chawki, Using X-ray images and deep learning for automated detection of coronavirus disease, J. Biomol. Struct. Dyn. (2020) 1–12, https://doi.org/10.1080/07391102.2020.1767212.

[15] S.R. Nayak, D.R. Nayak, U. Sinha, V. Arora, R.B. Pachori, Application of deep learning techniques for detection of COVID-19 cases using chest X-ray images: a comprehensive study, Biomed. Signal Process Control 64 (2021) 102365, https://doi.org/10.1016/j.bspc.2020.102365.

[16] S. Albahli, A deep neural network to distinguish covid-19 from other chest diseases using x-ray images, Current medical imaging 17 (1) (2021) 109–119, https://doi.org/10.2174/1573405616666200604163954.
[17] T. Ozturka, M. Talob, E.A. Yildirimc, U.B. Baloglud, O. Yildirime, U.R. Acharyafgh, Automated detection of COVID-19 cases using deep neural networks with X-ray images, Comput. Biol. Med. 121 (103792) (2020) 10–1016, https://doi.org/10.1016/j.compbiomed.2020.103792.
[18] G. Dhiman, V.V. Kumar, A. Kaur, A. Sharma, DON: deep learning and optimization-based framework for detection of novel coronavirus disease using X-ray images, Interdiscipl. Sci. Comput. Life Sci. (2021) 1–13, https://doi.org/10.1007/s12539-021-00418-7.
[19] S. Motamed, P. Rogalla, F. Khalvati, RANDGAN: randomized generative adversarial network for detection of COVID-19 in chest X-ray, Sci. Rep. 11 (1) (2021) 1–10, https://doi.org/10.1038/s41598-021-87994-2.
[20] H. Feng, Y. Liu, M. Lv, J. Zhong, A case report of COVID-19 with false negative RT-PCR test: necessity of chest CT, Jpn. J. Radiol. 38 (5) (2020) 409–410, https://doi.org/10.1007/s11604-020-00967-9.
[21] T. Ai, Z. Yang, H. Hou, C. Zhan, C. Chen, W. Lv, L. Xia, Correlation of chest CT and RT-PCR testing for coronavirus disease 2019 (COVID-19) in China: a report of 1014 cases, Radiology 296 (2) (2020) E32–E40, https://doi.org/10.1148/radiol.2020200642.
[22] C. Jin, W. Chen, Y. Cao, Z. Xu, Z. Tan, X. Zhang, J. Feng, Development and evaluation of an artificial intelligence system for COVID-19 diagnosis, Nat. Commun. 11 (1) (2020) 1–14, https://doi.org/10.1038/s41467-020-18685-1.
[23] J. Chen, K.C. See, Artificial intelligence for COVID-19: rapid review, J. Med. Internet Res. 22 (10) (2020), e21476, https://doi.org/10.2196/21476.
[24] L. Liu, D. Zhao, F. Yu, A.A. Heidari, C. Li, J. Ouyang, J. Pan, Ant colony optimization with Cauchy and greedy Levy mutations for multilevel COVID 19 X-ray image segmentation, Comput. Biol. Med. (2021) 104609.
[25] X. Pang, K. Gong, X. Zhang, S. Wu, Y. Cui, B.Z. Qian, Osteopontin as a multifaceted driver of bone metastasis and drug resistance, Pharmacol. Res. 144 (2019) 235–244.
[26] S. Zhao, P. Wang, A.A. Heidari, H. Chen, H. Turabieh, M. Mafarja, C. Li, Multilevel threshold image segmentation with diffusion association slime mould algorithm and Renyi's entropy for chronic obstructive pulmonary disease, Comput. Biol. Med. 134 (2021) 104427.
[27] G. Liu, W. Jia, M. Wang, A.A. Heidari, H. Chen, Y. Luo, C. Li, Predicting cervical hyperextension injury: a covariance guided sine cosine support vector machine, IEEE access 8 (2020) 46895–46908.
[28] Y. Li, L. Jiao, R. Shang, R. Stolkin, Dynamic-context cooperative quantum-behaved particle swarm optimization based on multilevel thresholding applied to medical image segmentation, Inf. Sci. 294 (2015) 408–422.
[29] E. Turajlić, Application of firefly and bat algorithms to multilevel thresholding of X-ray images, in: 41st International Convention on Information and Communication Technology, Electronics and Microelectronics (MIPRO), 2018, pp. 1104–1109.
[30] M. Abdel-Basset, V. Chang, R. Mohamed, HSMA_WOA: a hybrid novel Slime mould algorithm with whale optimization algorithm for tackling the image segmentation problem of chest X-ray images, Appl. Soft Comput. 95 (2020) 106642.
[31] J. Murillo-Olmos, E. Rodríguez-Esparza, M. Pérez-Cisneros, D. Zaldivar, E. Cuevas, G. Trejo-Caballero, A.A. Juan, Thresholding algorithm applied to chest X-ray images with pneumonia, in: Metaheuristics in Machine Learning: Theory and Applications, 2021, pp. 359–407.
[32] L. Abualigah, A. Diabat, P. Sumari, A.H. Gandomi, A novel evolutionary arithmetic optimization algorithm for multilevel thresholding segmentation of covid-19 ct images, Processes 9 (7) (2021) 1155.
[33] S. Chakraborty, A.K. Saha, S. Sharma, S. Mirjalili, R. Chakraborty, A novel enhanced whale optimization algorithm for global optimization, Comput. Ind. Eng. 153 (2021) 107086, https://doi.org/10.1016/j.cie.2020.107086.
[34] H. Chen, Y. Xu, M. Wang, X. Zhao, A balanced whale optimization algorithm for constrained engineering design problems, Appl. Math. Model. 71 (2019) 45–59.
[35] Y. Sun, T. Yang, Z. Liu, A whale optimization algorithm based on quadratic interpolation for high-dimensional global optimization problems, Appl. Soft Comput. 85 (2019) 105744.
[36] R.C. Gonzalez, R.E. Woods, Digital Image Processing, Prentice, 2006.
[37] P.K. Sahoo, S.A.K.C. Soltani, A.K. Wong, A survey of thresholding techniques, Comput. Vis. Graph Image Process 41 (2) (1988) 233–260.
[38] A.A. Aly, S. Bin Deris, N. Zaki, Research review for digital image segmentation techniques, Int. J. Comput. Sci. Inf. Technol. 3 (2011) 99–106.
[39] S.S. Chouhan, A. Kaul, U.P. Singh, Soft computing approaches for image segmentation: a survey, Multimed. Tool. Appl. 77 (21) (2018) 28483–28537.
[40] T. Kurban, P. Civicioglu, R. Kurban, E. Besdok, Comparison of evolutionary and swarm based computational techniques for multilevel color image thresholding, Appl. Soft Comput. 23 (2014) 128–143.
[41] S. Sarkar, S. Das, S.S. Chaudhuri, A multilevel color image thresholding scheme based on minimum cross entropy and differential evolution, Pattern Recogn. Lett. 54 (2015) 27–35.
[42] D. Oliva, M. Abd Elaziz, S. Hinojosa, Image segmentation using metaheuristics, in: Metaheuristic Algorithms for Image Segmentation: Theory and Applications, Springer, Cham, 2019, pp. 47–58.
[43] N. Otsu, A threshold selection method from gray-level histograms, IEEE transactions on systems, man, and cybernetics 9 (1) (1979) 62–66.
[44] J.N. Kapur, P.K. Sahoo, A.K. Wong, A new method for gray-level picture thresholding using the entropy of the histogram, Comput. Vis. Graph Image Process 29 (3) (1985) 273–285.
[45] S. Agrawal, R. Panda, S. Bhuyan, B.K. Panigrahi, Tsallis entropy based optimal multilevel thresholding using cuckoo search algorithm, Swarm and Evolutionary Computation 11 (2013) 16–30.
[46] Q. Askari, M. Saeed, I. Younas, Heap-based optimizer inspired by corporate rank hierarchy for global optimization, Expert Syst. Appl. 161 (2020) 113702.
[47] Y. Yang, H. Chen, A.A. Heidari, A.H. Gandomi, Hunger games search: visions, conception, implementation, deep analysis, perspectives, and towards performance shifts, Expert Syst. Appl. 177 (2021) 114864.
[48] S. Li, H. Chen, M. Wang, A.A. Heidari, S. Mirjalili, Slime mould algorithm: a new method for stochastic optimization, Future Generat. Comput. Syst. 111 (2020) 300–323.
[49] M.A. Elhosseini, A.Y. Haikal, M. Badawy, N. Khashan, Biped robot stability based on an A–C parametric whale optimization algorithm, Journal of Computational Science 31 (2019) 17–32.
[50] W. Sun, C. Zhang, Analysis and forecasting of the carbon price using multi—resolution singular value decomposition and extreme learning machine optimized by adaptive whale optimization algorithm, Appl. Energy 231 (2018) 1354–1371.
[51] C. Tang, W. Sun, W. Wu, M. Xue, A hybrid improved whale optimization algorithm, in: 2019 IEEE 15th International Conference on Control and Automation, ICCA), 2019, July, pp. 362–367.
[52] Q. Fan, Z. Chen, W. Zhang, X. Fang, ESSAWOA: enhanced whale optimization algorithm integrated with salp swarm algorithm for global optimization, Eng. Comput. (2020) 1–18.
[53] S. Chakraborty, A.K. Saha, S. Sharma, R. Chakraborty, S. Debnath, A hybrid whale optimization algorithm for global optimization, J. Ambient Intel. Humanized Comput. (2021) 1–37, https://doi.org/10.1007/s12652-021-03304-8.
[54] S. Sharma, A.K. Saha, A. Majumder, S. Nama, MPBOA-A novel hybrid butterfly optimization algorithm with symbiosis organisms search for global optimization and image segmentation, Multimed. Tool. Appl. 80 (8) (2021) 12035–12076, https://doi.org/10.1007/s11042-020-10053-x.
[55] S. Chakraborty, S. Sharma, A.K. Saha, S. Chakraborty, SHADE-WOA: A Metaheuristic Algorithm for Global Optimization, Applied Soft Computing, 2021, https://doi.org/10.1016/j.asoc.2021.107866, 107866.
[56] S.K. Elsayed, S. Kamel, A. Selim, M. Ahmed, An improved heap-based optimizer for optimal reactive power dispatch, IEEE Access 9 (2021) 58319–58336, https://doi.org/10.1109/ACCESS.2021.3073276.
[57] Z. Cui, X. Hou, H. Zhou, W. Lian, J. Wu, Modified slime mould algorithm via levy flight, in: 2020 13th International Congress on Image and Signal Processing, BioMedical Engineering and Informatics (CISP-BMEI), 2020, pp. 1109–1113.